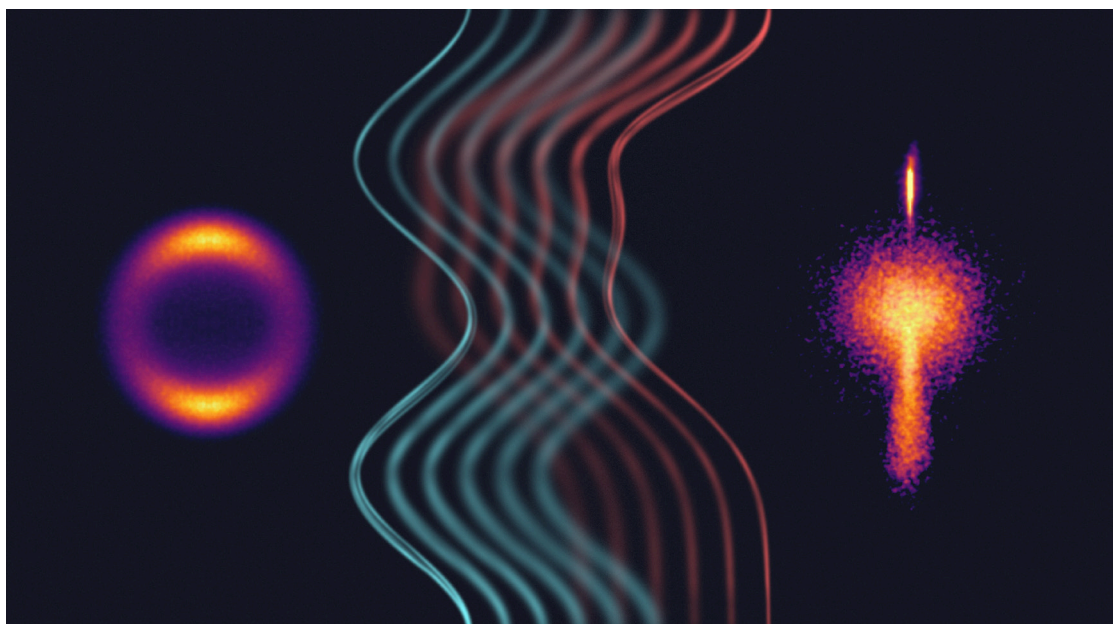


Doctoral Thesis in Chemical Engineering

Near-ambient pressure velocity map imaging

TZU-EN CHIEN



Near-ambient pressure velocity map imaging

TZU-EN CHIEN

Academic Dissertation which, with due permission of the KTH Royal Institute of Technology, is submitted for public defence for the Degree of Doctor of Philosophy on Wednesday the 21 February 2024 at 10:00 in room F3, KTH, Lindstedtsvägen 26, Stockholm.

Doctoral Thesis in Chemical Engineering
KTH Royal Institute of Technology
Stockholm, Sweden 2024

© Tzu-En Chien

Cover: An abstract illustration of images from NAP-VMI

TRITA-CBH-FOU-2023:62

ISBN: 978-91-8040-811-0

Printed by: Universitetsservice US-AB, Sweden 2024



〈定風波〉宋·蘇軾

三月七日，沙湖道中遇雨，雨具先去，同行皆狼狽，余獨不覺。
已而遂晴，故作此。

莫聽穿林打葉聲，何妨吟嘯且徐行。
竹杖芒鞋輕勝馬，誰怕？一蓑煙雨任平生。
料峭春風吹酒醒，微冷，山頭斜照卻相迎。
回首向來蕭瑟處，歸去，也無風雨也無晴。

Ding Feng Bo by Su Shi
Translate by Yang Xianyi and Gladys Yang

On the seventh day of the third month we were caught in the rain on our way
to Shahu. The umbrellas had gone ahead, my companions were downhearted,
but I took notice. It soon cleared, and I wrote this.

Forget that patter of rain on the forest leaves,
Why not chant a poem as we plod slowly on?

Pleasanter than a saddle this bamboo staff and straw sandals.
Here's nothing to fear.
I could spend my whole life in the mist and rain.

The keen spring wind has sobered me,
Left me chilly,
But slanting sunlight beckons from high on the hill;

One last look at scene behind
And on I go,
Impervious to wind, rain or sunny weather.

Near-ambient pressure velocity map imaging

Tzu-En Chien

Department of Chemical Engineering, KTH Royal Institute of Technology
SE-100 44 Stockholm, Sweden

Abstract

Catalytic reactions on solid surfaces have been studied under Ultra-high vacuum (UHV) conditions for decades. These studies provide crucial information for catalytic reactions, such as surface structures, adsorption sites, and reaction mechanisms. However, industrial catalysis operates under high gas pressure to increase the reaction rate, so the knowledge we learn from the previous UHV studies may not be able to directly transfer to the industry. This difference is referred to as the “pressure gap”, and it represents the difficulties that scientists encounter when attempting to investigate and comprehend catalytic reactions at high pressure. To address this issue, *in situ/operando* techniques and instruments have been developed to study reactions at pressures closer to real-world applications.

The present thesis aims to showcase the new instrument, Near-Ambient Pressure Velocity Map Imaging (NAP-VMI), and its applications to molecular spectroscopy and surface science at near-ambient pressures. This instrument features a velocity map imaging (VMI) setup with redesigned ion optics and uses differential pumping to achieve a working pressure of 10^{-3} mabr. It allows time-resolved measurements at microsecond time scales using the pump-probe technique with a pulsed molecular beam and a pulsed laser. The performance is validated using N_2O photodissociation and N_2 surface scattering. CO oxidation on Pd(110) and Pd(100) surfaces is studied at elevated oxygen pressure (1×10^{-5} mbar) where the surfaces reconstruct. The results show the suppression of CO_2 production in oxygen rich environments for both surfaces. The difference in kinetics and dynamics behavior between the two surfaces also suggests that surface structures and adsorption sites are important in the reaction mechanisms. These findings highlight the importance of surface structure in catalytic reactions and pave the way for more effective catalysts to be designed by tailoring surface properties and reaction conditions.

Key words: Catalyst, Surface reaction, Near-ambient pressure, CO, CO_2 , CO oxidation, Pd, Palladium, Instrument design, Velocity-map imaging

Näraomgivningstryck hastighetskarta avbildning

Tzu-En Chien

Institutionen för Kemiteknik, Kungliga Tekniska högskolan,
SE-100 44 Stockholm, Sverige

Sammanfattning

Katalytiska reaktioner på fasta ytor har studerats under ultrahögt vakuum (UHV) i årtionden. Dessa studier ger avgörande information för katalytiska reaktioner, såsom ytstrukturer, adsorptionsställen och reaktionsmekanismer. Industriell katalys arbetar dock under högt gastryck för att öka reaktionshastigheten, så kunskapen vi lär oss från de tidigare UHV-studierna kanske inte direkt kan överföras till industrin. Denna skillnad kallas "tryckgapet" och den representerar de svårigheter som forskare möter när de försöker undersöka och förstå katalytiska reaktioner vid högt tryck. För att lösa detta problem har *in situ/operando* metoder och instrument utvecklats för att studera reaktioner vid tryck som ligger närmare verkliga tillämpningar.

Den föreliggande avhandlingen syftar till att visa upp det nya instrumentet, nära-omgivande tryckhastighetskarta-avbildning (NAP-VMI) och dess tillämpningar för molekylär spektroskopi och ytvetenskap vid nära-omgivande tryck. Detta instrument har en hastighetskarta-avbildning (VMI) med omdesignad jonoptik och använder differentialpumpning för att uppnå ett arbetstryck på 10^{-3} mabr. Den tillåter tidsupplösta mätningar på mikrosekunders tidsskalor med hjälp av pump-probe-teknik med pulsmolekylär stråle och pulslaser. Prestandan valideras med hjälp av N_2O fotodissociation och N_2 ytspridning. CO oxidation på Pd(110) och Pd(100) ytan studeras vid förhöjt syretryck (1×10^{-5} mbar) där ytorna rekonstrueras. Resultaten visar undertryckandet av CO_2 produktion i syrerika miljöer för båda ytorna. Skillnaden i kinetik och dynamikbeteende mellan de två ytorna tyder också på att ytstrukturer och adsorptionsställen är viktiga i reaktionsmekanismerna. Dessa fynd framhäver vikten av ytstruktur i katalytiska reaktioner och banar väg för mer effektiva katalysatorer som kan utformas genom att skräddarsy ytegenskaper och reaktionsförhållanden.

Nyckelord: Katalysator, Ytreaktion, Näraomgivningstryck, CO, CO_2 , CO oxidation, Pd, Palladium, Instrumentdesign, Hastighetskartbildning.

Preface

This thesis presents the design and construction of near-ambient pressure velocity-map imaging for studying heterogeneous catalysis reactions under elevated pressure with μs time resolution. A brief introduction, an overview, the experimental setup, and the results are presented in Part I. Part II contains the three articles listed below. The articles have been adjusted to comply with the current thesis format for consistency, but their contents have not been altered as compared with their original counterparts.

Paper 1. TZU-EN CHIEN, LEA HOHMANN, AND DAN J. HARDING, 2022. *Near-ambient pressure velocity map imaging*. J. Chem. Phys. **157**, 034201.

Paper 2. TZU-EN CHIEN, LEA HOHMANN, AND DAN J. HARDING. *Time-Resolved Surface Reaction Kinetics in the Pressure Gap*. Submitted to Faraday Discussions.

Paper 3. TZU-EN CHIEN, LEA HOHMANN, AND DAN J. HARDING. *Bimodel Activity on Heterogeneous Catalysts: CO oxidation on Pd(100)*. Manuscript under preparation.

February 2024, Stockholm
Tzu-En Chien

Division of work between authors

The main supervisor for the project is Dan J. Harding (DJH) and Klas Engvall (KE) acts as co-supervisor.

Paper 1. The concept has been proposed by DJH. The design and construction have been conducted by Tzu-En Chien (TEC), DJH and Lea Hohmann (LH). The experiments and data analysis have been conducted by TEC. The paper has been written by DJH and TEC with feedback from LH.

Paper 2. The experiments and data analysis have been conducted by TEC and LH. The reaction model has been developed by TEC and LH. The paper has been written by TEC with feedback from DJH and LH.

Paper 3. The experiments and data analysis have been conducted by TEC. The reaction model has been developed by TEC and LH. The paper has been written by TEC with feedback from DJH and LH.

Other publications

The following papers co-authored by TEC are not included in this thesis.

LEA HOHMANN, KESS MARKS, TZU-EN CHIEN, HENRIK ÖSTRÖM, TONY HANSSON, MATTHIAS MUNTWILER, KLAS ENGVALL, MATS GÖTHELID, DAN HARDING, 2023. *The Effect of Co-adsorbed Sulfur on the Dehydrogenation of Naphthalene on Ni(111)*. Submitted to J. Phys. Chem. C..

Conferences

Part of the work in this thesis has been presented at the following international conferences. The presenting author is underlined.

TZU-EN CHIEN, LEA HOHMANN AND DAN J. HARDING. *The design and construction of a near-ambient pressure velocity-mapping imaging apparatus*. ISMB 2021 - International Symposium on Molecular Beams. Virtual (online), 2021.

TZU-EN CHIEN, LEA HOHMANN AND DAN J. HARDING. *Watch The Gap: Bridging the pressure gap in catalysis*. NCS 2022 - Nordic Symposium on Catalysis. Espoo, 2022.

Contents

Abstract	vii
Sammanfattning	viii
Preface	ix
 Part I - Overview and summary	
 Chapter 1. Introduction	1
1.1. Aims and scope of present thesis	2
1.2. Sustainability aspects	2
 Chapter 2. Background	4
2.1. Surface catalysis	4
2.2. Ultra-high vacuum techniques	6
2.3. Near-ambient pressure measurements	7
2.3.1. Non-charged particles methods	8
2.3.2. Scattering and charged particle methods	8
2.4. Velocity map imaging	9
2.5. CO adsorption and oxidation on Pd(110)	9
2.5.1. CO adsorption	10
2.5.2. O ₂ adsorption	11
2.5.3. CO oxidation	11
2.6. CO adsorption and oxidation on Pd(100)	12
2.6.1. CO adsorption	13
2.6.2. O ₂ adsorption	13
2.6.3. CO oxidation	13
 Chapter 3. Experimental setup and methods	16
3.1. NAP-VMI	17
3.1.1. Molecular beam chamber	17

3.1.2.	Scattering chamber	18
3.1.3.	Detector chamber	19
3.1.4.	Preparation chamber	20
3.1.5.	VMI ion optics	21
3.1.6.	Sample manipulator and sample holder	21
3.1.7.	STM chamber	22
3.2.	Molecule ionization	24
3.2.1.	Laser system	24
3.2.2.	REMPI	25
3.3.	Data treatment: VMI images	25
3.3.1.	Photodissociation	26
3.3.2.	Surface scattering	27
3.3.3.	Time-resolved measurement	29
3.4.	Data treatment: Kinetic models	30
3.4.1.	CO scattering	30
3.4.2.	CO oxidation	31
Chapter 4.	Results and Discussion	33
4.1.	NAP-VMI calibration and performance under NAP	33
4.1.1.	VMI simulation	33
4.1.2.	VMI calibration and performance	33
4.1.3.	VMI performance under NAP	34
4.2.	CO scattering and oxidation on Pd(110)	36
4.2.1.	CO scattering	36
4.2.2.	CO oxidation	36
4.2.3.	CO oxidation under oxygen rich environments	38
4.3.	CO scattering and oxidation on Pd(100)	41
4.3.1.	CO scattering	41
4.3.2.	CO oxidation	42
4.3.3.	CO oxidation: $p_{\text{O}_2} = 1 \times 10^{-6}$ mbar	44
4.3.4.	CO oxidation: $p_{\text{O}_2} = 1 \times 10^{-7}$ mbar	45
Chapter 5.	Conclusions and outlook	48
5.1.	Summary and conclusions	48
5.2.	Future work	49
5.3.	Outlook	51
Acknowledgements		52
Bibliography		53

Part II - Papers

Summary of the papers

63

Paper 1. Near-ambient pressure velocity map imaging

Paper 2. Time-Resolved Surface Reaction Kinetics in the Pressure Gap

Paper 3. Bimodel Activity on Heterogeneous Catalysts: CO oxidation on Pd(100)

Part I

Overview and summary

Introduction

Controlling chemical reactions is modern alchemy. Although we still cannot make gold out of nowhere, we can control reactions using catalysts. The term “catalysis” was coined by Swedish chemist Jöns Jacob Berzelius. He proposed the name based on the Greek words “kata” (down) and “lysis” (loosening) to describe the action of substances that speed up chemical reactions without being altered themselves (Berzelius 1835; Wisniak 2010).

Catalysts are everywhere, from mother nature to industrial manufacturing (Chorkendorff & Niemantsverdriet 2017; Norden 2014). Some examples of processes that employ catalysis in nature are: (1) enzymatic catalysis, which drives all of the biochemical reactions in living organisms; (2) in plants, the process of photosynthesis, where sunlight is captured to convert carbon dioxide and water into glucose and oxygen; (3) certain bacteria can convert atmospheric nitrogen into ammonia through nitrogen fixation; and (4) metal ion catalysis, which assists in substrate binding and stabilization of reaction intermediates.

Catalysts increase the efficiency of chemical reactions, reduce energy consumption, and often lead to cleaner and more sustainable production processes, which are essential in modern industry. For instance, (1) the Haber-Bosch Process uses iron catalysts to synthesize ammonia from nitrogen and hydrogen; (2) steam reforming uses nickel-based catalysts to convert methane and other hydrocarbons with steam into hydrogen and carbon monoxide; (3) selective catalytic reduction (SCR) uses vanadium- or titanium-based catalysts to reduce nitrogen oxides in flue gases with the aid of a reducing agent, typically ammonia or urea; (4) catalytic converters in vehicles use platinum, palladium, and rhodium as primary catalysts to reduce harmful emissions. They transform toxic gases like carbon monoxide, nitrogen oxides, and unburned hydrocarbons into less harmful substances such as water, nitrogen, and carbon dioxide; (5) electrocatalysis is used in hydrogen fuel cells, where platinum-based catalysts facilitate the splitting of hydrogen gas, while other catalysts like metal oxides can help with oxygen reduction; and additionally, (6) many modern synthetic routes to organic chemistry involve homogenous catalytic steps, often employing transition metal catalysts or enzymes. For example, cross-coupling reactions with metal-based catalysts are widely used in the synthesis of pharmaceuticals.

Heterogeneous catalysis refers to the type of catalysis process where the reactions take place at the interface between two phases, typically solid and gas. Studying the chemical reaction on a surface often requires a finely controlled environment, such as a vacuum condition. When investigating catalytic processes, researchers often use techniques that require ultra-high vacuum (UHV) conditions to achieve clear, uncontaminated results (Ertl 2001). However, industrial catalysis operates under high gas pressure to increase the reaction rate. This discrepancy is known as the “pressure gap”, where researchers face challenges when trying to study and understand catalytic reactions under high pressure (Frenken & Groot 2017). This difference in pressure conditions means that the behavior and characteristics observed for catalysts in the laboratory under UHV conditions might not always align with industrial circumstances. For example, under high pressure environments, catalysts might have different active sites, or the rate-determining step of a reaction might change. To address this issue, researchers have been developing techniques and instruments that allow them to study catalysts at pressures closer to those of real-world applications. In summary, the “pressure gap” emphasizes the importance of studying catalysts under conditions that mirror real-world applications, ensuring that the findings are relevant and can be used to design and develop better catalytic processes.

1.1. Aims and scope of present thesis

The present thesis aims to showcase the new method, Near-Ambient Pressure Velocity Map Imaging (NAP-VMI), and its capabilities for surface science and molecular spectroscopy under near-ambient pressure conditions, which are sufficient to cause surface reconstructions (Tao *et al.* 2010). We demonstrate the application of NAP-VMI to the study of CO oxidation on palladium model surfaces, resolving a long-standing debate concerning the active phase in oxygen-rich environments in previous research.

The thesis begins with an introduction to surface reactions and techniques to study them under UHV and near-ambient pressure; the working principle of velocity map imaging (VMI); CO oxidation on Pd(110) and Pd(100), which we use as model systems in our studies. The following chapter focuses on the design, assembly of the machine, and experimental methods. The first section of the results chapter demonstrates how the new ion optics design, combined with differential pumping, allows the experiments to be conducted at pressures of 10^{-3} mbar (**Paper 1**). In the later section of the results chapter, we present the time-dependent measurements of CO oxidation on Pd(110) and Pd(100) surfaces. These measurements, conducted under elevated pressures, highlight the changes in surface structures and provide kinetic information on these meta-stable surfaces (**Paper 2 & 3**).

1.2. Sustainability aspects

Catalysts play an essential role in advancing sustainability in various sectors. By facilitating chemical reactions to occur more efficiently and under milder

conditions, catalysts can lead to processes that are more energy efficient, produce fewer waste products, and use fewer resources. For sustainability goals to be met, continuous research and investment in catalysis are necessary. For instance, creating less expensive, non-noble metal catalysts that are more environmentally friendly requires an understanding of how reactions work. This way, industries can use more common materials instead of rare, toxic and expensive ones, making their processes more affordable and eco-friendly. It's not just about developing new catalysts, but also about understanding their mechanisms, improving their lifetimes, and making their production more sustainable.

In the aspect of this thesis, catalytic oxidation of CO falls into several categories of UN Sustainable Development Goals (SDG), primarily by contributing to better air quality, public health, sustainable energy, and environmental protection. **SDG 3, Good Health and Well-Being:** Effective CO oxidation enhances urban air quality, contributing to healthier, more sustainable living spaces. It helps to reduce air pollution by converting harmful CO from vehicle exhaust and industrial emissions into less harmful CO₂. **SDG 11, Sustainable Cities and Communities:** Despite the fact that CO₂ is a greenhouse gas, converting CO to CO₂ reduces the overall greenhouse effect because CO reacts with hydroxyl (OH) radicals, reducing their abundance in the atmosphere. CO indirectly increases the global warming potential because OH radicals help to reduce the lifetimes of strong greenhouse gases like methane and CO₂. Additionally, understanding the catalytic reaction mechanisms indirectly contribute to **SDG 9, Industry, Innovation, and Infrastructure:** Advancements in the catalysis processes promote industrial innovation, paving the way for more sustainable and efficient production methods with reduced environmental footprints.

Background

This chapter provides general information about the chemical reactions on surfaces and the techniques used to study surfaces in ultra-high vacuum and near-ambient pressure conditions. It is followed by a brief description of the conventional VMI technique and an overview of CO adsorption and oxidation on Pd(110) and Pd(100) surfaces.

2.1. Surface catalysis

Surface catalysts reduce the reaction energy barrier, creating a new reaction path for molecules. From a molecular point of view, several elementary steps are involved in the reaction. Typically, two reaction mechanisms have been proposed for metal surface reactions (Baxter & Hu 2002). The first is the Langmuir-Hinshelwood (L-H) mechanism. The general steps for the L-H mechanism are as follows: (1) adsorption of the reactant molecules; (2) reaction (formation of products); and (3) desorption of the product molecules. The second mechanism is the Eley-Rideal (E-R) mechanism. The E-R mechanism assumes that only one of the molecules adsorbs and the other one reacts directly from the gas phase without adsorption. In practice, the E-R mechanism rarely exists; therefore, we only consider the L-H mechanism in the following discussion. Here are some key factors that control surface reactivity.

- Adsorption: Before the reaction can proceed, the reactant molecules need to be adsorbed onto the catalyst's surface. An adsorption site on a catalyst is a location where reactant molecules or atoms can bind or "adsorb". Sticking probability refers to the probability that a gas molecule or atom impinging upon a solid surface will adsorb (stick) to the surface instead of reflecting back into the gas phase. The sticking probability usually decreases with surface coverage, which refers to the fraction of adsorption sites on a surface that are occupied by adsorbate. Surface coverage is often discussed in unit of monolayer (ML). The common definition of 1 ML is equal to one adsorbate adsorbs on one surface atom.
- Desorption: The desorption rate controls the residence time of adsorbates. The residence time for reactants should be sufficiently long to allow them to react or to diffuse to the active sites and then react. However, the desorption rates for the products should be fast enough so that the

catalyst is not poisoned. For simple first-order processes, the desorption rate can be described as a function of temperature and desorption activation energy using the Arrhenius equation:

$$k_{\text{desorption}}(T_s) = A \cdot e^{\frac{-E_d}{k_b T_s}} \quad (2.1)$$

where A is the pre-exponential factor, E_d is the desorption activation energy, T_s is the surface temperature, and k_b is the Boltzmann constant.

- **Reaction:** The surface reaction rate quantifies how fast the reactants undergo a reaction after they have adsorbed onto the catalyst surface. The surface reaction rate is often expressed in terms of the surface coverage of the adsorbed species. For a simple bi-molecular reaction $A + B \rightarrow P$, the reaction rate is given by:

$$rate_{\text{product}} = k_r \theta_A \theta_B \quad (2.2)$$

where k_r is the reaction rate constant and θ_A and θ_B are the surface coverage of species A and B, respectively. The surface reaction rate typically depends on temperature, often described by the Arrhenius equation:

$$k_r(T_s) = A \cdot e^{\frac{-E_a}{k_b T_s}} \quad (2.3)$$

where A is the pre-exponential factor, E_a is the reaction activation energy, T_s is the surface temperature, and k_b is the Boltzmann constant.

- **Potential energy diagram:** From an energy perspective, a potential energy diagram, also known as a reaction coordinate diagram, shows how the energy of a system changes as a chemical reaction proceeds. Figure 2.1 shows a typical potential energy diagram for a reaction both with and without catalysts. The transition state is the highest energy point on the minimum energy reaction pathway and corresponds to the state of the system as it transforms from reactants to products. The activation energy (E_a) is the energy difference between the initial state and the transition state, representing the energy barrier that needs to be overcome to proceed with the reaction. Catalysts function by offering an alternative reaction pathway with a reduced activation energy compared to the non-catalytic reaction, making it easier for reactants to achieve the transition state and to form products.
- **Reaction steps:** In a sequence of reactions, such as adsorption, surface reaction, and desorption, the slowest step dictates the overall rate. This slowest step is called the rate-determining step. In a complex system, competitive reactions might happen. Competitive reactions refer to processes where two or more pathways or reactions compete for the same reactants. Understanding the intricacies of the elementary steps allows chemists to manipulate reaction conditions or design novel catalysts to achieve desired outcomes in terms of yield and selectivity.

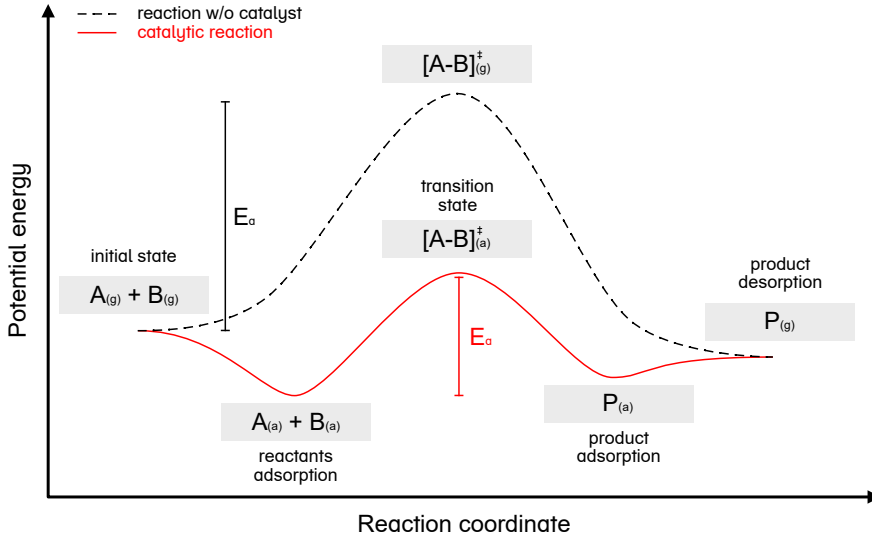


Figure 2.1: Comparison of the potential energy diagram for catalytic and non-catalytic reactions.

2.2. Ultra-high vacuum techniques

Ultra-high vacuum (UHV) conditions are crucial for surface science studies. UHV refers to very low pressures, typically below 10^{-9} mbar. The use of UHV offers a controlled environment that keeps the surface clean for the duration of an experiment period (several hours). UHV provides an environment that surfaces can be studied in their intrinsic state without the complications introduced by contaminants or excessive gas-surface interactions. In addition, many surface sensitive techniques, which involve the detection of charged particles, require operation under UHV conditions. In the context of the present thesis, some important UHV techniques and methods are:

- **Auger Electron Spectroscopy (AES):** AES is a surface analytical technique used to determine the elemental composition of surfaces. It can analyze the top few atomic layers of a material, making it ideal for investigating surface compositions and checking if the surface is contaminated. The process of AES begins by bombarding a sample with an electron beam, which ionizes atoms. This ionization creates electron vacancies that are filled by electrons from the same atom. This relaxation transition emits another electron, known as an Auger electron. The kinetic energy of these emitted Auger electrons is characteristic of specific elements, allowing for their identification.

- **X-ray Photoelectron Spectroscopy (XPS):** XPS is a technique that uses X-rays to emit core electrons from a sample. By measuring the kinetic energy of the emitted electrons, XPS provides detailed information about the sample’s elemental composition and chemical states at the surface (several nm in depth).
- **Low-Energy Electron Diffraction (LEED):** LEED is a technique utilized to determine the atomic structure of crystalline surfaces. By directing a beam of low-energy electrons at a surface and observing the resulting diffraction pattern on a detector, the periodicity and symmetry of the surface atoms can be deduced. While LEED provides insights about surface reconstructions, adsorption sites, and surface phase transitions, it requires surfaces with a consistent, repeating pattern over a large area (long range order) to perform effectively.
- **Scanning Tunneling Microscopy (STM):** STM is an atomic-scale imaging technique rooted in the quantum tunneling principle. By bringing a sharp metallic tip close to a conductive surface and applying a bias voltage, a tunneling current forms, which is highly sensitive to the tip–surface distance. This allows STM to produce detailed topographic images with atomic resolution. STM is capable of visualizing individual atoms and studying molecular arrangements.
- **Reflection Absorption Infrared Spectroscopy (RAIRS):** RAIRS is a surface-sensitive technique designed to investigate the vibrational modes of molecules adsorbed on metal surfaces. Using infrared radiation directed at a grazing angle, RAIRS detects specific frequencies absorbed by the molecules, revealing their vibrational characteristics. This makes it especially valuable for analyzing molecule-surface interactions and adsorption sites.
- **Temperature-Programmed Desorption (TPD):** Unlike the techniques mentioned above, which study the surface structures, TPD is a method that investigates desorbed molecules into gas phase. In a UHV environment, a sample with adsorbed species is methodically heated, causing the species to desorb. By monitoring the desorbed concentration of species as a function of temperature, a desorption spectrum is derived, revealing binding energies and desorption kinetics. This technique is widely used to understand surface binding energies, reaction mechanisms, and adsorbate interactions.

2.3. Near-ambient pressure measurements

Near-ambient pressure (NAP) studies or *operando* studies bridge the gap between fundamental UHV surface science and real-world applications (Frenken & Groot 2017). Detection techniques without charged particles, such as STM, and optical methods like PM-IRAS and surface X-ray diffraction can be easily adapted to NAP. Here we will briefly review recently developed NAP detection methods.

2.3.1. *Non-charged particles methods*

- Scanning Tunneling Microscope (STM): Although STM can operate under high pressure, there are technical problems when performing under high pressure and high temperature. Elevated temperatures lead to an increase in thermal drift, causing drift in the images. The piezo element, which controls the STM tip, must remain below its Curie temperature. This is not easy to achieve under high pressure due to the convective flow causing temperature rises. In most high pressure STM designs, there is a small volume high pressure cell. In this configuration, only the STM tips and surfaces are exposed to the high pressure (Tao *et al.* 2008; Herbschleb *et al.* 2014).
- Planar Laser Induced Fluorescence (PLIF): PLIF is an optical technique using a laser sheet, which is a planar and thin sheet of laser light, to excite a section of the sample; the subsequent fluorescence emitted can be correlated to local concentrations. It is often employed in fluid dynamics, but when applied to catalysis, it offers real-time visualization of reactive species distribution over a catalyst surface (Zetterberg *et al.* 2012; Blomberg *et al.* 2015, 2016b).
- Surface Optical Reflectance (SOR): SOR techniques analyze the reflectivity of light from catalyst surfaces to deduce properties and reactions occurring on them. Changes in reflectivity can indicate molecular adsorption, surface oxidation, or other reactions. SOR is valuable for observing surface changes in real-time and in 2D imaging (Zhou *et al.* 2017).

2.3.2. *Scattering and charged particle methods*

- X-ray Photoelectron Spectroscopy (XPS): XPS traditionally operates under ultra-high vacuum (UHV) conditions. There are a few problems that need to be overcome to work under high pressure. The emitted photoelectrons have a very short mean free path in high pressure gases. At atmospheric pressures, the photoelectrons can undergo scattering or be absorbed before reaching the detector, leading to signal loss. To minimize the flight distance at high pressure, the path between the sample and the entrance of the detector is shortened by adding an aperture right above the surface (hundreds of μm); multiple differential pumping stages to minimize electron scattering in the electron flight region. The other issue is the discharge through the gas where high voltage differences are present, as in the electrostatic lens system or the electron detectors. Differential pumping with a better lens design is used to address these questions (Salmeron & Schlögl 2008).
- Environmental Molecular Beam (EMB) technique: EMB, which was developed at the University of Gothenburg to facilitate scattering experiments on volatile liquids employs an aperture to distinguish between the high pressure surface area and the low-pressure zone near the detector (Kong *et al.* 2012).

- Transmission Electron Microscopy (TEM): High Pressure TEM operates based on the fundamental principles of traditional TEM but includes modifications to accommodate samples under non-vacuum conditions. The working principle of HP-TEM involves enclosing the sample between two ultra-thin, electron-transparent windows. These create a miniature sealed chamber or micro-reactor, which can be filled with a gas or liquid, allowing the sample to exist under elevated pressures, mimicking real-world conditions (Chee *et al.* 2020).

2.4. Velocity map imaging

Velocity map imaging was first used by Eppink & Parker (Eppink & Parker 1997). It is a powerful experimental technique used in atomic and molecular physics to study the dynamics of ions or electrons in photoionization or photodissociation processes induced by lasers. It provides a way to measure the speed and angular distribution of charged particles simultaneously. Figure 2.2 shows the working principle of a VMI. Traditional VMI ion optics have three electrodes (repeller, extractor and ground). Charged particles created in a region of interest are accelerated by an electric field towards a detector. If the particles have the same initial velocity, they will hit the detector at the same spot, regardless of their original spatial locations. The result is an image on the detector where each spot corresponds to a particular velocity. The position on the detector indicates the projection of the velocity vector, and the distance from the center indicates the speed. Many groups have been working on improving the resolution (time and space) by slicing techniques (Ashfold *et al.* 2006) or a high speed camera (Bromberger *et al.* 2022). DC slicing and pulsed slicing are techniques that increase the flight time of the ions/electrons, which results in the ions/electrons spreading out, forming a longer packet. This spreading makes it easier to analyze since a short voltage pulse at the detector can be used for selecting the center of the ion packet. Laser slicing selects the molecules of interest with a point or sheet laser, reducing the space charge effect and improving the kinetic energy resolution.

While VMI has been used in a wide range of gas phase experiments, the focus of this thesis is more specific in gas-solid interactions. In many recent studies (Hadden *et al.* 2016; Harding *et al.* 2017; Greenwood & Koehler 2021), a method that combines VMI with molecular beam and surface scattering techniques is used to study gas-solid interactions.

2.5. CO adsorption and oxidation on Pd(110)

In the results section (Section 4.2), we studied the CO scattering and oxidation on the Pd(110) surface with NAP-VMI. Therefore, we briefly review the Pd(110) surface structures upon the adsorption of CO, O₂, and during CO oxidation at UHV and (near) ambient pressure conditions in the following sections.

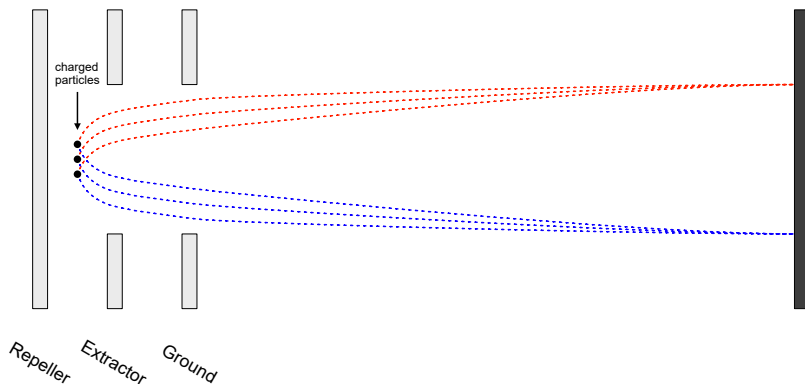
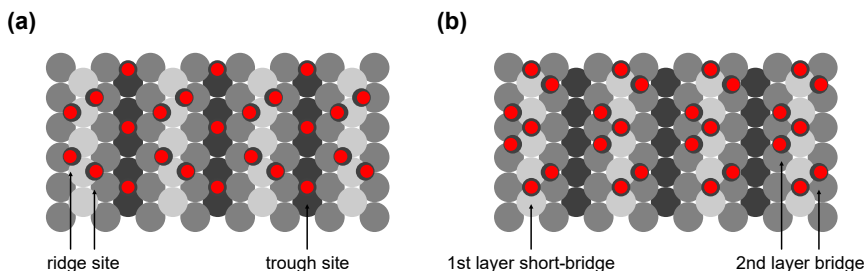


Figure 2.2: VMI working principle.

2.5.1. CO adsorption

At room temperature, CO molecularly adsorbs onto Pd(110) and can induce a (1×2) -missing row reconstruction. When the CO coverage is low ($\theta_{\text{CO}} < 0.3$), CO adsorption appears random on the (1×1) pristine surface. As CO coverage increases ($0.3 < \theta_{\text{CO}} < 0.75$), Pd(110) undergoes a transition into a (1×2) -missing row pattern, leading to a $c(4 \times 2)$ -CO structure. Two different CO adsorption structures are proposed by Raval *et al.* and Zhang *et al.*. Raval *et al.* suggested that CO molecules can attach both on the ridge and the trough sites; and Zhang *et al.* suggested CO adsorbs on the first layer of Pd at short-bridge positions and on the second layer at bridge sites. Figure 2.3 shows the two structures proposed by (a) Raval *et al.* and (b) Zhang *et al.* (Raval *et al.* 1990; Zhang *et al.* 2011).

Figure 2.3: CO/Pd(110)-missing row structures proposed in (a) (Raval *et al.* 1990) and (b) (Zhang *et al.* 2011).

2.5.2. O_2 adsorption

Oxygen adsorbs dissociatively on Pd(110) at temperatures above 160 K, leading to the formation of several structures, including $p(1 \times 3)$, $p(1 \times 2)$, (2×3) -1D, $c(2 \times 4)$, $c(2 \times 6)$, and complex surface oxide structures at different temperatures and oxygen exposures. The oxygen-induced reconstructions of Pd(110) are complex, but the $c(2 \times 4)$ has received the most interest. This specific structure has a Pd(110) surface (1×2) -missing row structure, with oxygen atoms adsorbed on the ridge rows in a zigzag pattern. The $c(2 \times 4)$ structure is found at oxygen pressure as low as 10^{-8} mbar and remains up to pressure around 10^{-7} mbar. With further increase in oxygen pressure, the anti-phase domain boundaries populate the missing-row structure. When oxygen pressure reaches 1×10^{-6} mbar, the entire missing row structure is occupied. Figure 2.4 shows the $c(2 \times 4)$ -O structure and anti-phase domain boundaries on (1×2) -missing row Pd(110) (Goschnick *et al.* 1986; Westerström *et al.* 2009). Further increase in oxygen pressure gives rise to the $(7 \times \sqrt{3})$ and $(9 \times \sqrt{3})$ complex surface oxide structures.

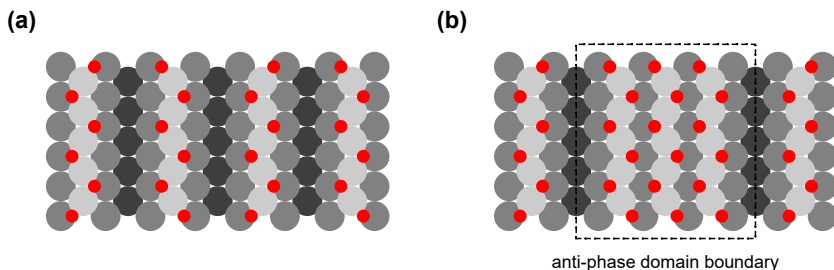


Figure 2.4: O_2 /Pd(110)-missing row structures; (a) $c(2 \times 4)$ -O structure and (b) anti-phase domain boundaries on (1×2) -missing row Pd(110).

2.5.3. CO oxidation

CO oxidation on Pd(110) has been examined both in traditional UHV environments and in *operando* settings. Some key findings from the previous studies:

- Ladas *et al.* conducted titration experiments of CO oxidation on an oxygen covered Pd(110) surface detected by LEED. The results showed that high oxygen coverages inhibit the rate of CO_2 production, which can be attributed to low CO adsorption activation energy or low CO sticking coefficient (Ladas *et al.* 1993).
- Yasui *et al.* studied CO oxidation on the Pd(110) $c(2 \times 4)$ -O surface by TPD combining EELS and LEED, suggesting that the CO molecules

approach O-atoms at the peripheries of $c(2 \times 4)$ -O surface patches (Yasui *et al.* 1998).

- RAIRS of CO oxidation on Pd(110) $c(2 \times 4)$ -O surface showed that once surface temperature is above 250 K, CO molecules move from atop and bridge sites to only bridge sites (Fukui *et al.* 1996).
- Early XPS experiments showed that O₂ dissociative adsorption was inhibited by CO pre-covered Pd(110) surface (Jones *et al.* 1999).
- Matsushima’s group reported the investigations of the velocity and angular distribution of the desorbing CO₂ from CO oxidation on Pd(110). They found two desorbing components with slow and fast speed. The slow component has a wider angular distribution; and the fast component has narrower angular distribution (Wako *et al.* 2000; Moula *et al.* 2001; Yamanaka 2008).
- PM-IRAS studies by Gao *et al.* observed a transient peak in CO₂ turnover frequency (TOF) right after the “light-off” region, which later stabilizes at a lower rate due to mass transfer limitations (MTL), and they claimed that the Pd reduced metal phase is the most active phase at both low and high pressure (Gao *et al.* 2009b).
- NAP-XPS studied CO oxidation on Pd(110) under sub-Torr conditions and showed that CO poisoning occurs at low surface temperatures ($< 165^\circ\text{C}$ / 438 K). Above this temperature, CO molecules desorb while the surface is dominated by chemisorbed oxygen (surface oxide) with a small amount of PdO bulk oxide. The CO₂ production is proportional to the amount of chemisorbed oxygen, which they indicated as the active phase and followed the L-H mechanism (Toyoshima *et al.* 2013; Kondoh *et al.* 2016).
- PLIF studies of CO oxidation on Pd(110) suggested that the CO partial pressure variation within the boundary layer will affect the structure and activity of the catalyst, which should be considered for *in situ* studies (Blomberg *et al.* 2015, 2016a).

Many of these investigations have divergent findings due to different measurement techniques and reactor configurations. Most of the groups (Toyoshima *et al.* 2013; Kondoh *et al.* 2016) directly correlated the surface structures under high oxygen pressure to their reactivity, leading to the conclusion that surface oxide is the active phase. Contrarily, Gao and colleagues claimed that the Pd reduced metal phase is the most active phase (Gao *et al.* 2009b; van Rijn *et al.* 2010; Gao *et al.* 2010).

2.6. CO adsorption and oxidation on Pd(100)

In the results section (Section 4.3), we studied the CO scattering and oxidation on the Pd(100) surface with NAP-VMI. Therefore, we briefly review the Pd(100) surface structures upon the adsorption of CO, O₂, and during CO oxidation at UHV and (near) ambient pressure conditions in the following sections.

2.6.1. CO adsorption

CO adsorbed on Pd(100) exhibits a single vibrational feature, throughout the temperature range 80–600 K and pressure range $p_{\text{CO}} = 1 \times 10^{-6} - 1$ Torr (Ortega *et al.* 1982; Szanyi *et al.* 1993; Ozensoy & Goodman 2004). The characteristic of this vibration mode is assigned to Pd-CO birdge vibration. At $\theta_{\text{CO}} = 0.5$, CO forms an ordered structure of $(2\sqrt{2} \times \sqrt{2})R45^\circ - 2\text{CO}$ (Behm *et al.* 1980). Ouvrard *et al.* reported a uncommon atop CO from sum frequency generation (SFG) at 300 K and $p_{\text{CO}} = 0.5$ Torr (Ouvrard *et al.* 2014).

2.6.2. O₂ asorption

Oxygen adsorbs dissociatively on the Pd(100) and results in several ordered structures: $\text{p}(2 \times 2)\text{-O}$ ($\theta_{\text{O}_2} = 0.25$), $\text{c}(2 \times 2)\text{-O}$ ($\theta_{\text{O}_2} = 0.5$), $\text{p}(5 \times 5)\text{-O}$ ($\theta_{\text{O}_2} = 0.64$) and $(\sqrt{5} \times \sqrt{5})R27^\circ\text{-O}$ ($\theta_{\text{O}_2} = 0.8$) (Chang & Thiel 1987, 1988a; Chang *et al.* 1988; Chang & Thiel 1988b; Zheng & Altman 2002b). The $(\sqrt{5} \times \sqrt{5})R27^\circ\text{-O}$ structure (denoted as $(\sqrt{5} \times \sqrt{5})\text{-O}$) can be considered as a strained single layer of PdO(101) on the Pd(100) surface. It also appears in a wide range of temperatures and pressures (Todorova *et al.* 2003; Lundgren *et al.* 2004; Kostelník *et al.* 2007; Shipilin *et al.* 2014, 2017). Further increase the oxygen pressure promote the growth of the epitaxial multilayer oxide (Seriani *et al.* 2009; Rijn *et al.* 2011; Shipilin *et al.* 2015; Mehar *et al.* 2023). A non-epitaxial layer of bulk-like PdO was observed at $p_{\text{O}_2} > 0.5$ mbar (Westerström *et al.* 2011). In a recent report (Mehar *et al.* 2023), the oxidation of Pd(100) by oxygen forms an epitaxial multilayer PdO(101) at 500 K. At temperatures above 600 K, the growth of PdO(100) along with PdO(101) results in a thicker and rougher oxide.

2.6.3. CO oxidation

Due to the complexity of the metal-oxide structures, the CO oxidation on the Pd(100) has been extensively investigated. Key findings from previous studies that focused on catalytic activity and surface structures:

- Hendriksen *et al.* studied CO oxidation on Pd(100) using STM. The Pd(100) reversibly oxidizes and reduces by a oxygen rich flow or CO rich flow, respectively. The reduced surface is flat, and the oxidized surface is rough. The CO oxidation reaction rate increases with the formation of an oxidized surface. They suggested the reaction takes place on the metal surface and follows the L-H mechanism; the oxide surface follows the Mars–Van Krevelen mechanism, where the oxide is continuously consumed by CO and reformed under oxygen rich conditions (Hendriksen *et al.* 2004, 2010).
- Gao *et al.* disagreed with the interpretation of Hendriksen *et al.*. They claimed that the reduced metal is the most active phase at both low and high pressure because they observed a transient peak in CO₂ turnover frequency (TOF) right after the “light-off” region, which later stabilizes at a lower rate due to mass transfer limitations (MTL). Additionally,

they observed a new CO vibration mode associated with O-atoms at oxygen rich environments ($O_2/CO > 5$) after the “light-off” region (Gao *et al.* 2009*b,a*).

- Zheng & Altman performed the titration experiments on oxygen covered Pd(100) toward reduction by CO using LEED, TPD, TPR, and STM. LEED showed that the $(\sqrt{5} \times \sqrt{5})$ -O surface structure is reduced by CO and results in the (2×2) -O structure. At high surface temperatures ($> 450K$), a long delay is observed before the redaction starts. The reduction lag on the $(\sqrt{5} \times \sqrt{5})$ -O surface is due to the slow reduction of the $(\sqrt{5} \times \sqrt{5})$ -O surface, indicating that the oxidized surface is less active. TPR results showed that the inactivity is due to the inability to adsorb CO (Zheng & Altman 2002*a*).
- (N)AP-XPS investigations into the CO oxidation on Pd(100) have been reported by several groups (Toyoshima *et al.* 2012; Blomberg *et al.* 2013; Gustafson *et al.* 2018; Yu *et al.* 2019; Blomberg *et al.* 2021; Knudsen *et al.* 2021; Goodwin *et al.* 2021). Toyoshima *et al.* observed the CO_2 formation increased with the formation of O-Pd-O trilayer surface oxide, suggesting the upper O species of the surface oxide is the key to high activity. Yu *et al.* agree with the finding of Toyoshima *et al.*. Blomberg *et al.* reported the CO oxidation on Pd(100) up to 1 bar. A metallic Pd is observed after “light-off” in the highly active region. The difference between the results compared to previous reports might be due to the reactor design and the gas flow configuration. Gustafson *et al.* suggested that the thin PdO oxide films are at least as active as metallic surfaces, and the unsaturated metal oxide can act as active sites. Goodwin *et al.* used grazing incidence X-ray photoelectron spectroscopy to highlight the structure of the metallic islands formed on top of the oxide island should be considered. Knudsen *et al.* performed the time-resolved AP-XPS with the combination of gas pulse and event-averaging with the time resolution in seconds, which is the time scale for phase transition. They reported that a transient metallic surface is highly active for CO oxidation.
- CO oxidation has also been studied by computational theory methods such as Density Functional Theory (DFT) and First-principles Kinetic Monte Carlo (1p-kMC) simulation (Rogal *et al.* 2007*a,b*, 2008; Hoffmann & Reuter 2014; Hoffmann *et al.* 2015; Matera *et al.* 2015). They developed the microkinetic model and aimed to understand the stable Pd(100) surface structures during CO oxidation at different temperatures and pressures, as well as to describe the experiments on a macroscale.
- PLIF study with 1p-kMC suggested a phase mixture (metallic Pd(100) and $(\sqrt{5} \times \sqrt{5})$ -O surface oxide) during CO oxidation on Pd(100) (Matera *et al.* 2015).
- CO oxidation and reduction of the Pd oxides are studied at UHV conditions using Temperature Programmed Reaction Spectroscopy (TPRS), RAIRS, and DFT (Weaver *et al.* 2015, 2017; Kim *et al.* 2018; Mehar

et al. 2018). The results show that chemisorbed O/Pd(111) is 2–3 times more reactive than the PdO(101)/Pd(111) surface (Weaver *et al.* 2017), while a multilayer PdO(101)/Pd(100) is more active than a single layer PdO(101)/Pd(100) (Mehar *et al.* 2018). Additionally, they suggested that the oxidation reaction on the metal oxide follows the Mars–van Krevelen (MvK) mechanism, and the oxygen vacancies play an important role in CO oxidation.

- Two-dimensional surface optical reflection (2D-SOR) showed that no PdO bulk oxide was formed; instead, a well-defined surface oxide was formed during CO oxidation on the Pd(100) surface. The study combined with PM-IRRAS showed the desorption of CO with the formation of a surface oxide (Rämisch *et al.* 2022).

The formation of oxides, which can act as active phases for CO oxidation, complicates CO oxidation on Pd(100) more than on Pd(110). Despite extensive investigation, questions about surface structures and active phases still remain. Additionally, none of these studies had good time resolution to measure reaction kinetics, with the exception of Knudsen *et al.*. As a result, additional research will be required in the future.

Experimental setup and methods

The development of a new method and the design and construction of an appropriate instrument were the main focus of present thesis. The experiments presented in this thesis were conducted with a home-built apparatus named Near-Ambient Pressure Velocity Map Imaging (NAP-VMI) at KTH. The general concept and design are published in **Paper 1** (Chien *et al.* 2022). The NAP-VMI apparatus is designed for investigating molecular beam surface scattering in conditions ranging from ultra-high vacuum (fundamental surface science) to near ambient pressure (applied catalysis). This unique setup bridges the “pressure gap”, enabling the study of chemical reaction dynamics and kinetics in scenarios where higher pressures are essential or unavoidable. Figure 3.1 shows the photo and CAD design of the apparatus.

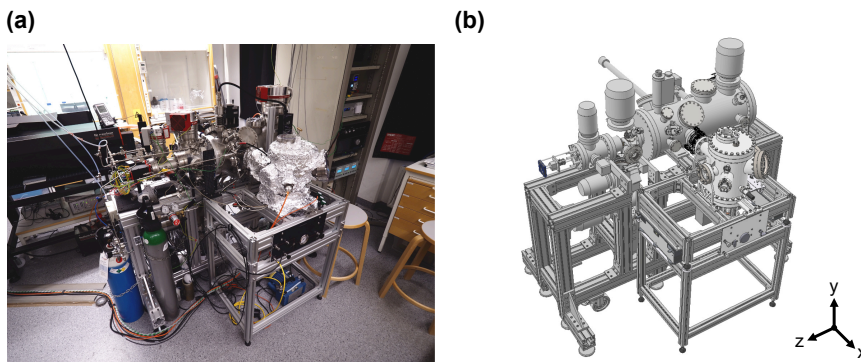


Figure 3.1: (a) photo and (b) CAD model of the NAP-VMI apparatus.

It is equipped with several turbomolecular pumps, maintaining a base pressure in the chamber below 2×10^{-9} mbar. However, during experiments, the pressure inside the scattering chamber can reach 1×10^{-3} mbar. We use differential pumping techniques to separate the microchannel plate (MCP) detector, which operates exclusively in high vacuum, from the high pressure

region. The present chapter describes the comprehensive design of the NAP-VMI instrument, experimental methods, and general kinetic models for the surface reactions.

3.1. NAP-VMI

The NAP-VMI apparatus consists of the following main components:

- Molecular beam chamber: The molecular beam chamber generates the supersonic molecular beam, initiating the gas-surface reaction.
- Scattering chamber: The surface and VMI optics are located in the scattering chamber, where the reaction takes place.
- Detector chamber: The detector chamber contains a MCP detector, which is used to detect ions produced when molecules are ionized by a laser during scattering and/or reactions.
- Preparation chamber: The preparation chamber is used for sample transfer and sample preparation. A sample manipulator is located in this chamber.
- STM chamber: The scanning tunneling microscope (STM) chamber mounted next to the preparation chamber.
- Laser system: Tunable laser light for ionizing the target molecules is achieved by tripling the frequency of a Dye laser's fundamental, pumped by a frequency doubled Nd:YAG laser.

Figure 3.2 shows a cross-sectional view of the NAP-VMI in the y-z plane, with the components labeled.

3.1.1. Molecular beam chamber

The standard method for generating molecular beams with well defined velocities involves a supersonic expansion into a vacuum followed by differential pumping. Using a pulsed valve minimizes the pumped gas volume by producing a brief, concentrated molecular beam. This is achieved by expanding gas from a high pressure reservoir through a small nozzle into low pressure or vacuum. Figure 3.3 shows the design of the molecular beam source chamber. It consists of two chambers, the source chamber (LewVac, standard CF100 four way cross) and the differential chamber (our own design manufactured by VACOM), separated by a skimmer (Beam Dynamics Inc., Model 1 with a 2 mm opening) and pumped by a 350 and a 90 l/s turbomolecular pump (Leybold), respectively. The molecular beam chamber is mounted below the scattering chamber, separated by a 3 mm aperture (in the scattering chamber). A pulsed valve (Amsterdam Piezovalve, ACPV2 model) (Irimia *et al.* 2009) is mounted in the source chamber. The pulse valve has a 200 μm diameter and a 40-degree conical nozzle shape. The orifice of the nozzle is closed by a piezoelectric cantilever controlled by an electronic driver unit (Amsterdam Piezovalve, EDU5), allowing operation at a 10 Hz repetition rate with an opening duration of 20–400 μs . A typical backing gas pressure of 1–3 bar is used in the experiment. With the pulsed valve in operation, the pressure of the source chamber increases to 5×10^{-6} mbar, the

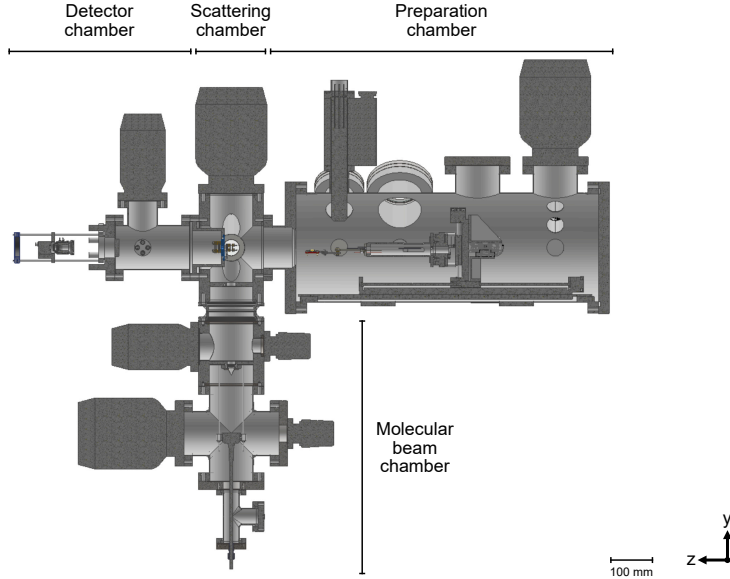


Figure 3.2: Cross section view in the y-z plan of the NAP-VMI.

pressure of the differential chamber increases to 1×10^{-7} mbar, and the pressure change in the scattering chamber increases is 3×10^{-9} mbar. Pressures in the source chamber and differential chamber are measured by full range vacuum gauges (Pfeiffer Vacuum, PKR 251); pressures in the scattering chamber are measured by cold cathode gauges (Pfeiffer Vacuum, IKR 270) in each chamber. This increase in pressure of 3×10^{-9} mbar with the 10 Hz valve running and a pumping speed of 350 l/s in the 3 l scattering chamber represents a load of 1×10^{-9} bar·l/s. Therefore, we estimate approximately 10^{12} molecules to reach the scattering chamber per pulse.

3.1.2. Scattering chamber

Figure 3.4 shows the design of the scattering chamber (our own design manufactured by VACOM). The scattering chamber is the “center” of the instrument, where the VMI ion optics are located (see Section 3.1.3 and 3.1.4); the molecular beam and laser cross each other at the VMI optics. It has four CF100 flanges, two CF63 flanges, and four CF40 flanges. It is pumped by a CF 100 turbomolecular pump (Pfeiffer Vacuum, 300 l/s) from the top. The molecular beam chamber is connected from below. Two CF100 flanges on the sides are connected to the preparation chamber and detector chamber, respectively. The laser beam coming from the side CF63 flanges with deep UV (DUV) viewports (LewVac). Four CF40 flanges are connected to a leak valve (LewVac), a high

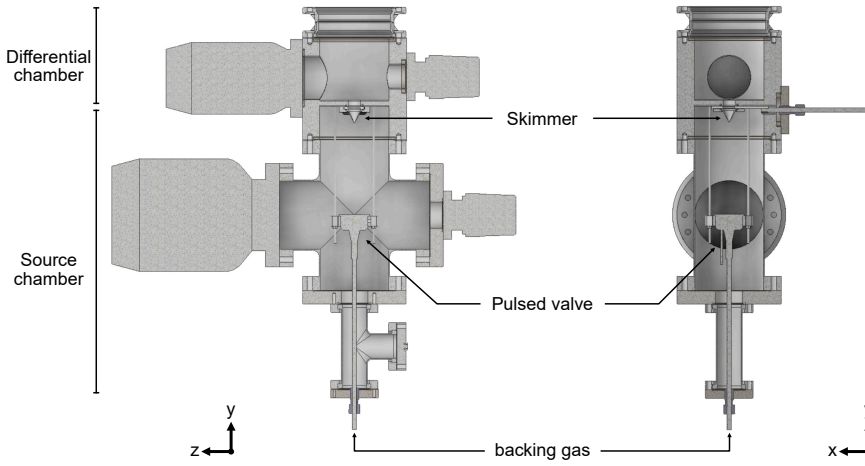


Figure 3.3: CAD model of the molecule beam chamber.

voltage feedthrough (LewVac) for ion optics, a cold cathode gauge (Pfeiffer Vacuum, IKR 270) and a blank flange, respectively.

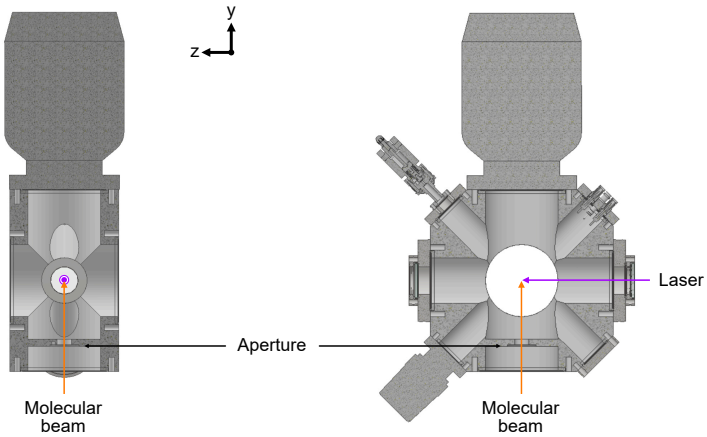


Figure 3.4: CAD model of the scattering chamber.

3.1.3. Detector chamber

Figure 3.5 shows the design of the detector chamber (our own design manufactured by VACOM). The detector chamber consists of a top hat shape CF100 flange, a VMI module (see Section 3.1.5), a flight tube, and a vacuum imaging

detector (Photek). The detector chamber is pumped by a CF63 turbomolecular pump (Pfeiffer Vacuum, 300 l/s). An inverted magnetron cold cathode gauge (Pfeiffer Vacuum, IKR 360) is used to reduce the influence of magnetic fields. A metal mesh in the ions' flight region is used to shield the electric field from the high voltage connections and feedthroughs. The flight distance for ions is 260 mm from the ionization center. The vacuum imaging detector has a 40 mm Z-stack MCPs with a P46* phosphor screen with a typical maximum working pressure of 10^{-6} mbar. Ions reach the MCPs and produce a cascade of electrons, which are accelerated onto the phosphor screen, where they emit light. A short high voltage gate pulse can be applied to the MCPs, allowing the targeted ions to be selected by their time-of-flight or m/z ratio and reducing background noise. A CCD camera (FLIR, 1.3 megapixel) with an 8 mm lens is used to capture the emitted light on the phosphor screen.

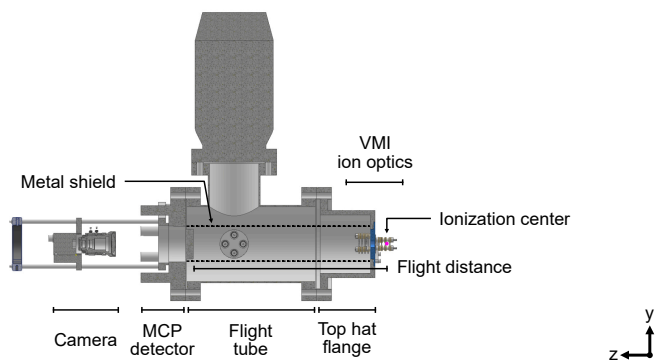


Figure 3.5: CAD model of the detector chamber and the ion optics.

3.1.4. Preparation chamber

Figure 3.6 shows the design of the preparation chamber (our own design manufactured by VACOM). The preparation chamber is a CF250 tube with several flanges. It is pumped by a CF100 turbomolecular pump (Pfeiffer Vacuum, 820 l/s). It is equipped with an Argon ion source (PREVAC, IS40C1), an Auger electron spectroscopy (AES) (RBD Instrument, microCMA), a residual gas analyzer (Extorr, XT100), two motor control feedthroughs (Arun Microelectronics), an electrical feedthrough (LewVac) and a thermocouple feedthrough (LewVac). A XYZR manipulator (see Section 3.1.6) is located in the preparation chamber. The sample cleaning process before experiments proceeds as follows: (1) Argon sputtering for 10 minutes at 3 keV and 5 mA ($8 \mu\text{A}$ at the surface), (2) annealing to 970 K for 5 minutes, and (3) natural cooling down to 400 K. After cleaning, an Auger analysis is conducted to check the sample's cleanliness.

*In **Paper 1**, we mentioned that a P43 phosphor screen was used, which was incorrect.

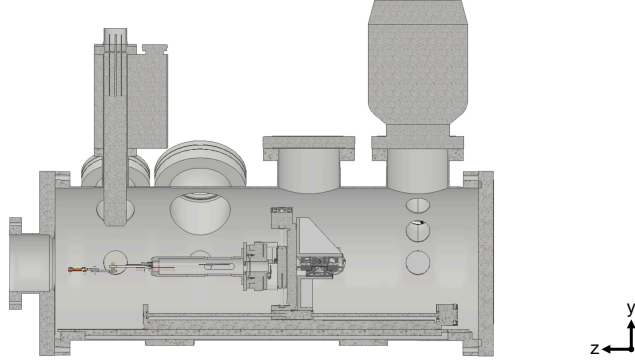


Figure 3.6: CAD model of the preparation chamber.

3.1.5. VMI ion optics

We aim to design VMI optics to reach a working pressure of 10^{-3} mbar. At this pressure, collisions between gas molecules become significant. The mean free path (λ) is the average distance a particle travels between collisions with other particles, which can be described as: $\lambda = kT/2\sigma P$, where k is the Boltzmann constant, T is the temperature, σ is the effective cross-section of the particle, and P is pressure. The mean free path at room temperature for air molecules at a pressure of 10^{-3} mbar is around 100 mm. For ions, σ is much bigger, which means the mean free path is shorter; therefore, it is very important to reduce the flight distance in the NAP region. To minimize the scattering effects of background molecules, the VMI ion optics need to be compact. Figure 3.7 shows the design of the VMI ion optics. The concept of the special VMI optics is to separate the high pressure scattering region from the detector chamber while ions still reach the detector with the proper velocity mapping feature. Eight electrodes (1 mm in thickness) are used in the ion optics, where four of them are in the scattering chamber and four of them are in the detector chamber, separated by a 3 mm pinhole. The first set of electrodes (R, E1, E2, and G) produce a hard focus of the ions at the aperture, and the second set of electrodes (F1, F2, F3, and F4) function as an acceleration region and an Einzel lens that fine tunes the focusing.

3.1.6. Sample manipulator and sample holder

Figure 3.8 shows the XYZR manipulator and sample holder. The XYZR manipulator consists of four UHV stepper motor stages (Arun Microelectronics). Three linear stages (X: 50 mm; Y: 50 mm; Z: 400 mm) and a rotational stage are joined by the homemade brackets and mounted in the preparation chamber. It

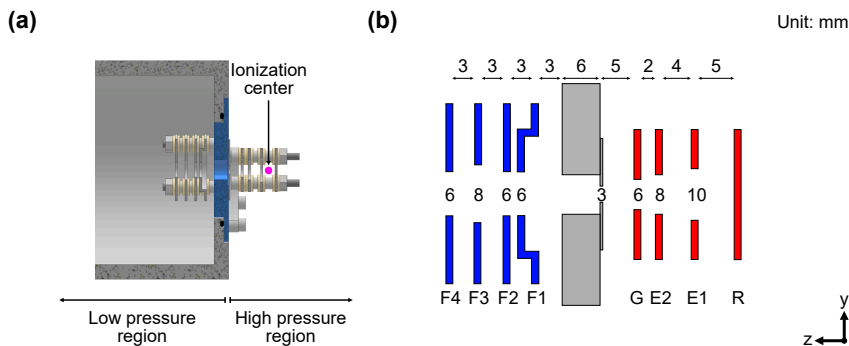


Figure 3.7: CAD model of the VMI ion optics.

allows the sample to move between the preparation chamber and the scattering chamber.

Due to the compact design of the VMI optics, we could not find a suitable commercial sample holder. Therefore, we also designed the sample holder. The criteria for the sample holder are:

- Compact design
- Heating up to 1000 K
- Measuring the surface temperature
- Capable of applying potential up to 500 V
- Use a removable flag style sample plate

Figure 3.9 shows the sample holder design and assembly, taking into account these criteria. Four different materials are used in the sample holder based on several factors, such as cost, functionality, and accessibility. The sample plate receiver is made of stainless steel 316Ti. The sample is heated from below by a pyrolytic graphite heating element (Thermic Edge), which is covered and insulated by pyrolytic boron nitride (pBN). The sample is mounted on a “flag-style” sample plate. Chromel–Alumel (type-K) thermocouple wire on the alumina bridge, which is connected by tantalum (Ta) thermocouple springs to the thermal couple feedthrough. In the current setup, we cannot simultaneously apply potential to the sample holder and measure surface temperature because they share the same connection, which poses a safety concern. We leave a tiny channel between the sample receiver and sample plate, allowing an isolated temperature measurement below the sample plate.

3.1.7. STM chamber

Figure 3.10 shows the connection of the NAP-VMI and STM. The reactor STM (Leiden Probe Microscopy) is installed in a separate chamber connected to the

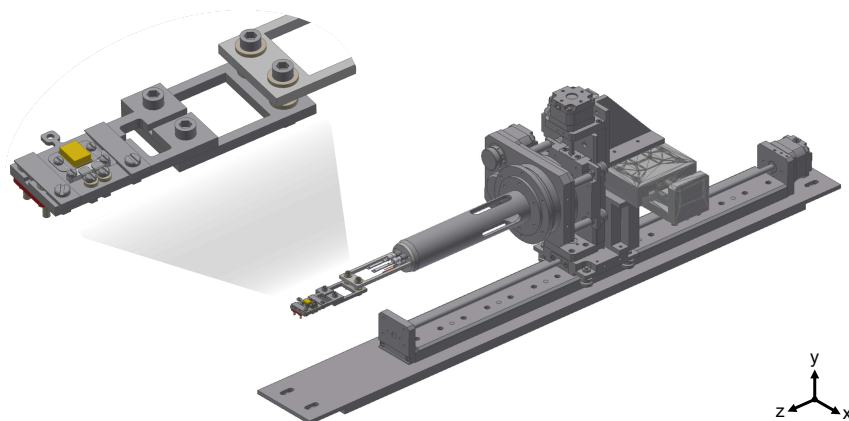


Figure 3.8: CAD model of the sample manipulator.

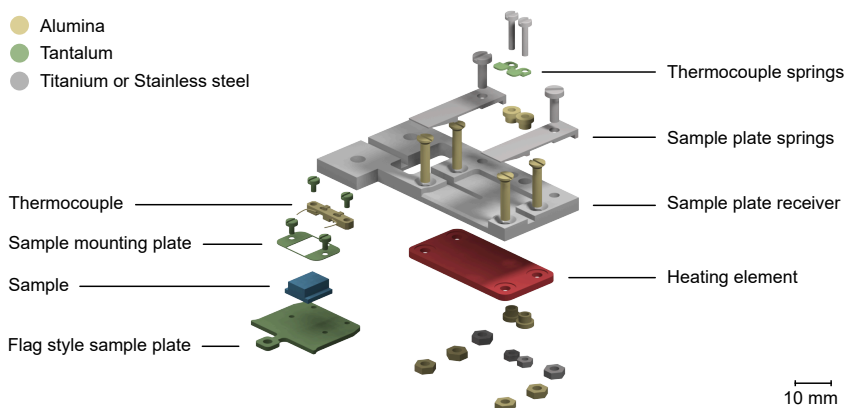


Figure 3.9: CAD model of the sample holder.

preparation chamber via a CF63 flexible coupling to minimize vibration originating from the preparation chamber. On the opposite side of the preparation chamber, a transfer arm was installed for transferring the flag style sample plate. Owing to delays in the STM delivery and installation, experiments with the STM were not conducted as part of this thesis. However, it is intended for studying surface structures under reaction conditions.

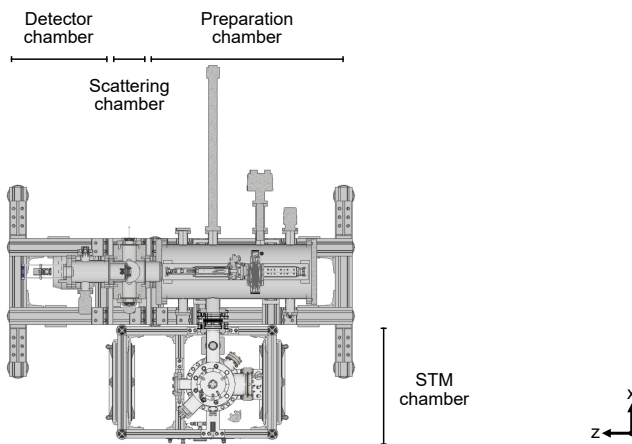


Figure 3.10: CAD model of the NAP-VMI and the STM chamber (Top view with cross section from the sample plan).

3.2. Molecule ionization

VMI optics velocity mapped the ions to the detector. In order to detect the neutral molecules in the experiments with VMI, they must first be ionized. We used a UV laser to ionize the target molecules.

3.2.1. Laser system

Figure 3.11 shows the diagram of the laser system. For ionization, laser light in the ultraviolet (UV) region (203–216 nm) is used. The flash lamp pumped Nd:YAG laser (InnoLas, SpitLight Compact) is frequency doubled, resulting in a wavelength of 532 nm and a repetition rate of 10 Hz. This frequency pumps the dye laser (Radiant Dyes, NarrowScan, DCM dye in ethanol). The dye laser comprises a resonator to select a specific wavelength in the dye mixture's gain profile, along with two amplifying stages to boost power. Each stage is pumped by a portion of the incoming 532 nm light. A 2400 lines/mm grating is used for choosing the desired wavelength. The amplified laser is frequency tripled with two BBO crystals, with the output wavelength in the UV region. Two Pellin–Broca prisms are used to separate the harmonics of the laser beam. A beam block blocks the fundamental and second harmonic lasers. Typical laser power output is around 1 mJ per pulse (measured after the Pellin–Broca prisms), with a pulse width of several ns. A variable wave plate (optional) controls the polarization of the laser. The laser is guided by several mirrors and focused in the center of the VMI optics by a 200 mm focal length lens.

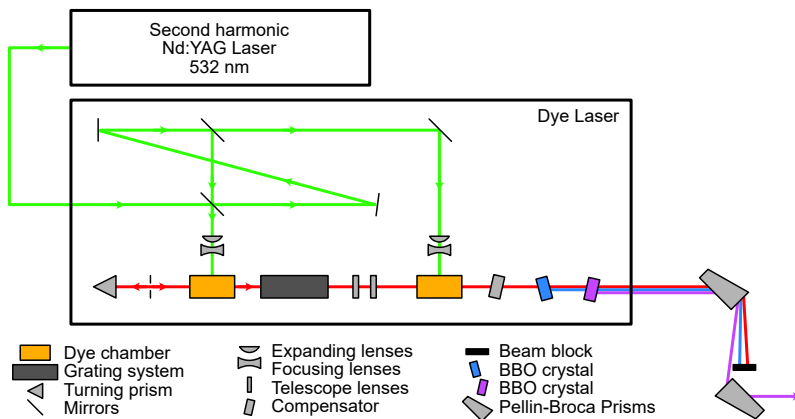


Figure 3.11: Schematic diagram of the laser system.

3.2.2. REMPI

Resonance-enhanced multiphoton ionization (REMPI) is used for ionization. The principle of REMPI is to ionize molecules through an intermediate resonant state. Figure 3.12 shows a typical 2+1 REMPI scheme. The 2+1 REMPI process needs two photons from the initial state to reach the resonant intermediate state and a third one overcome the ionization threshold and ionize. The resonant step makes it selective, and often quite efficient. Even minor laser power fluctuations can result in significant variations in the resulting ion signal.

In the later chapter (Chapter 4), N_2 , CO , and CO_2 are studied. N_2 molecules are ionized by 2+1 REMPI through the two-photon electronic transition $a'' \ ^1\Sigma_g^+ \leftarrow X \ ^1\Sigma_g^+$ at the laser wavelength around 203 nm (Lykke & Kay 1991). CO molecules are ionized using a 2+1 REMPI process via the $E \ ^1\Pi \leftarrow X \ ^1\Sigma^+$ transition at the laser wavelength around 215 nm (Hines *et al.* 1990). We use the $S(10)$ transition for the detection of scattered molecules, as the $J=10$ state is barely populated in the incident beam but is one of the most populated in the scattered distribution. CO_2 is detected using laser ionization around 212 nm. We expect this to be a 2+1 REMPI process, presumably via 1-photon-forbidden $^1\Sigma_g^+$ and/or $^1\Pi_g$ Rydberg states (Wu *et al.* 1991; Inn *et al.* 2004; Chan *et al.* 1993; McGlynn *et al.* 1971; Hubin-Franskin *et al.* 1988; Stark *et al.* 2007).

3.3. Data treatment: VMI images

The VMI ion optics map the velocity of the ions at the ionization region to a two-dimensional imaging sensor, which corresponds to their “velocity” before they were ionized. The center of the velocity map image represents ions have zero velocity in the x-y plane. The velocity map image includes speed (distance

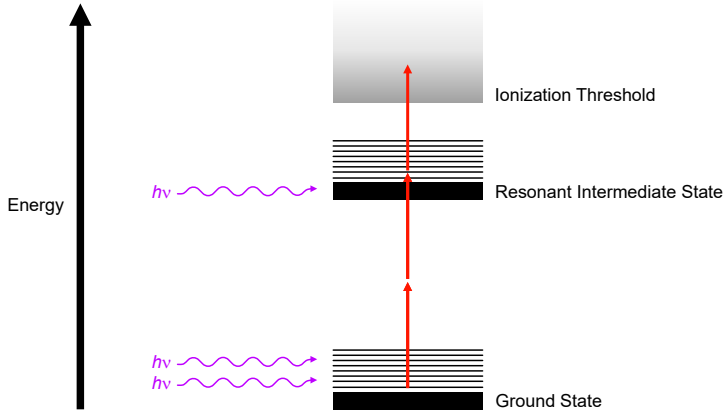


Figure 3.12: Schematic diagram of a 2+1 REMPI process.

from the center) and angular (direction from the center) information. We used several Python packages (Numpy, Scipy, and PyAbel) to analyze the images.

3.3.1. Photodissociation

Photodissociation experiments are used to test the performance of NAP-VMI and speed calibration. Photodissociation of N_2O around 203 nm produces rotationally excited N_2 fragments (Hanisco & Kummel 1993; Suzuki *et al.* 1996; Neyer *et al.* 1999; Nishide & Suzuki 2004; Kawamata *et al.* 2006) that can be rotational state selectively detected using 2+1 REMPI through the two-photon electronic transition $a''^1\Sigma_g^+ \leftarrow X^1\Sigma_g^+$ (Lykke & Kay 1991). The N_2 ion cloud in the shape of a sphere is projected onto the detector. Abel transform is an integral transform used in the analysis of axially symmetric functions. It takes a slice of a cylindrically symmetric 3D object and provides the 2D projection of that object. The inverse Abel transform takes a 2D projection and reconstructs a slice of the cylindrically symmetric 3D distribution. In analyzing the VMI of the N_2O photodissociation (Section 4.1.3), we did not use the inverse Abel transformation to reconstruct a slice of the spherically symmetric 3D distribution ion cloud. Using the 2-stage acceleration, the ion optics spread the arrival time of the ions at the detector depending on the particle motion in the z-axis. We applied a short high voltage gate pulse to the MCP detector (Section 3.1.3) and only selected the center part of the ion cloud (DC slice), from which we then acquired the speed and angular information directly without any mathematical treatment. The slicing technique also works without the need for cylindrically symmetry for inverse Abel transform. Figure 3.13 compares the VMIs of N_2 fragments ($J=74$) from N_2O photodissociation with different image treatments, Left: full ion cloud projection; Middle: inverse

Abel transformation image from the full ion cloud projection; Right: DC sliced image.

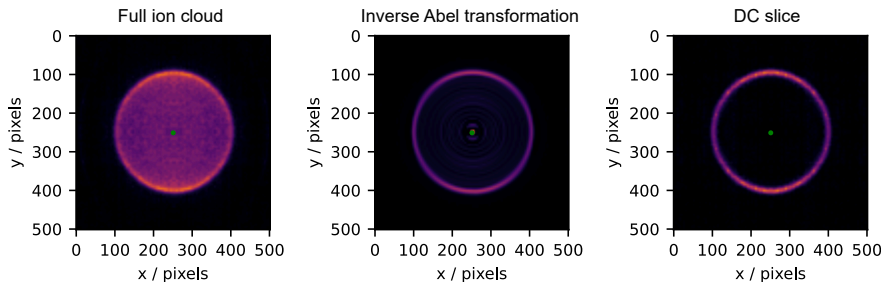


Figure 3.13: VMIs of N_2 fragments ($J=74$) from N_2O photodissociation. Left: full ion cloud projection; Middle: inverse Abel transformation image from the full ion cloud projection; Right: DC sliced image.

3.3.2. Surface scattering

Figure 3.14 shows a VMI of N_2 scattering on the Pd(110) surface at $T_s = 300$ K. The image consists of three parts: the incident beam, scattered molecules, and background molecules. The green cross in the image center represents the thermal background of N_2 molecules, which we also use to identify the zero-velocity point; the upper signal ($V_x > 0$) is the incident beam, which is traveling upward (approaching the surface), and the lower signal ($V_x < 0$) belongs to scattered molecules, which are traveling downward (leaving the surface) after scattering.

Some issues need to be considered when doing surface scattering experiments. (1) **Angular distribution:** Due to the compact design of the VMI optics, only scattered molecules in close proximity to the surface normal reach the ionization center. In **Paper 1** (Chien *et al.* 2022), we determined an angular acceptance of ± 25 degrees for surface scattering. The angular acceptance might be smaller according to results of the CO scattering on the Pd(110) surface. The angular detection for scatter molecules are limited by the geometric configuration of the molecular beam, the surface, and VMI ionization center. The surface to the ionization point is typically 15 mm and hole for the E1 electrode 10 mm. The in-plane (x - y plane) angular acceptance is mainly determined by the size of the molecular beam radius, laser ionization volume, and the VMI region, shows in figure 3.15. We estimate that only molecules within $\pm 15^\circ$ of the scattering plane parallel to the electrodes and detector will be ionized, which prevents us from measuring angular distributions for the scattering products. Detecting scattered molecules with full angular distribution is important for the kinetic models. Enhancing the angular acceptance will be a key focus for future improvements.

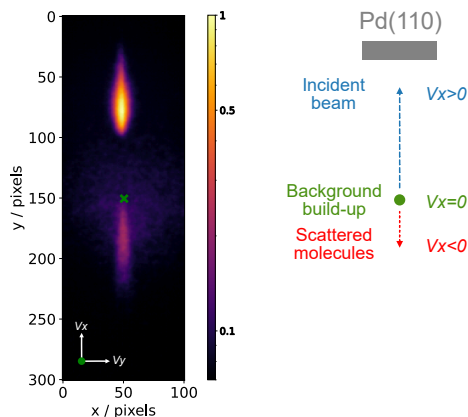


Figure 3.14: VMI of N_2 scattering on the Pd(110) surface at $T_s = 300$ K.

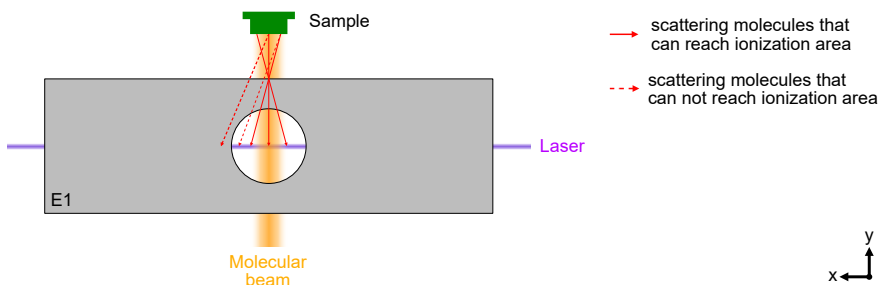


Figure 3.15: The geometric configuration of the molecular beam, the surface, and VMI ionization center.

(2) **Flux correction:** The signal is dependent on the gas density, which is inversely proportion to their speed. Therefore, a density to flux transformation is applied by multiplying the signal intensity by their speed accordingly.

The speed distribution can be described as a Maxwell-Boltzmann distribution of the surface temperature or as a flowing Maxwell-Boltzmann distribution (Hurst *et al.* 1979; Janda *et al.* 1980).

$$\text{Maxwell-Boltzmann distribution: } Flux(v) \propto v^3 \left(\frac{m}{kT_s}\right)^{\frac{3}{2}} \exp\left(-\frac{mv^2}{2kT_s}\right)$$

$$\text{Flowing Maxwell-Boltzmann distribution: } Flux(v) \propto v^3 \exp\left(-\frac{(v - v_0)^2}{\alpha^2}\right)$$

$Flux(v)$ is the flux as a function of velocity; m is the molecular mass of the target molecule; k is the Boltzmann constant; T_s is the surface temperature; v_0 is the flow velocity; and $\alpha^2 = 2kT_H/m$ (T_H is the characteristic temperature in the frame of reference moving with velocity V_0). For a better comparison to the previous reports (Wako *et al.* 2000; Moula *et al.* 2001), the average energy of the flowing Maxwell-Boltzmann distribution can be expressed in the temperature unit as $T_{fmb} = \langle E \rangle / 2k$, where $\langle E \rangle$ is the mean energy.

3.3.3. Time-resolved measurement

Time-resolved experiments use a delay generator (Berkeley Nucleonics Corporation, Model 577) to synchronize the delay time of the laser pulse, molecular beam valve, MCP detector, and camera. Figure 3.16 shows the time-synchronization scheme for the time-resolved measurement. The laser pulse is set as t_0 . The pulsed valve is set at a negative time, t_d , ahead of the laser due to the travel time of the gas pulse to reach the ionization center. The laser pulse and the molecular pulse meet at t_0 , and molecules are ionized. The MCP gate pulse is set at t_g which is the flight time of the target ions. The camera trigger is also set ahead of t_0 , due to the delay in computer communication with the camera. In a time-resolved measurement, images are obtained by scanning t_d .

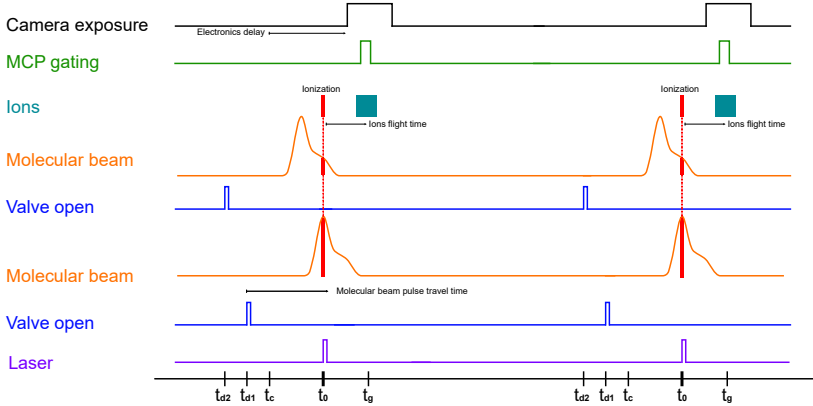


Figure 3.16: Time delay scheme for the time-resolved measurement.

Figure 3.17 shows how we convert a series of single-delay images (Figure 3.17(a)) to a kinetic trace. We recorded images while varying the delay between the pulsed molecular beam and the pulsed laser. Figure 3.17(b) shows the time-resolved measurement of CO scattering on Pd(110) (**Paper 2**), with each data point collected from an individual molecular-beam delay image, as shown in figure 3.17(a). For the CO scattering signals, we selected a region spanning 40–60 pixels and a 20-degree sector below the center (indicated by a green box).

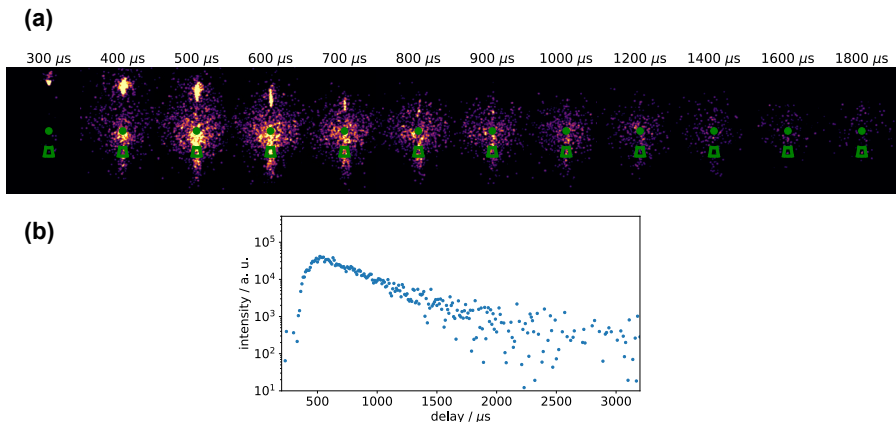


Figure 3.17: Time-resolved measurement from (a) a series of VMIs to (b) a kinetic trace.

3.4. Data treatment: Kinetic models

Kinetic models are used to describe the time-resolved measurement for different chemical processes. The methods we use to determine the time-dependent kinetics of surface reactions are based on the Velocity Resolved Kinetics (VRK) method developed in Alec Wodtke’s group in Göttingen (Golibrzuch *et al.* 2015; Harding *et al.* 2017). Velocity resolved detection allows the time-dependent flux of desorbing molecules with a certain velocity to be determined by physically deconvoluting the surface residence time from the spread in flight time from the surface to the ionization region.

In this section, we describe general kinetic models for CO scattering and CO oxidation. The complex kinetic models for each surface, which are modified based on our experimental results and previous reports, will be provided in Section 4.2 and 4.3.

3.4.1. CO scattering

There are two types of scattering on the gas–solid interaction (Rettner *et al.* 1996). (1) direct scattering: the incoming molecules directly reflect in an inelastic single collision; (2) trapping desorption: the incoming molecules trap on the surface, followed by a complete equilibration at the surface, and later desorb. The speed distribution of trapping desorption is a Maxwell-Boltzmann distribution characterized by the surface temperature.

Both processes occur for CO scattering on Pd surfaces, and the CO scattering flux, $\phi_d(t, T_s)$ comprises two components: the first is direct scattering, and the second is trapping desorption (Rettner *et al.* 1996; Golibrzuch *et al.* 2015; Harding *et al.* 2017). The kinetic model of the CO scattering flux can be

described with equation (3.1).

$$\phi_d(t, T_s) = \underbrace{A_{DS} \phi_i(t)}_{\text{direct scattering}} + \underbrace{A_{TD} k_d(T_s) [CO_{(a)}]_t}_{\text{trapping desorption}} \quad (3.1)$$

A_{DS} and A_{TD} represent the branching factors for direct scattering and trapping desorption, respectively. $\phi_i(t)$ is the time-dependent dosing function for the molecular beam, which is modeled by two Gaussian functions:

$$\phi_i(t) = A_1 e^{-\frac{(t-t_1)^2}{w_1^2}} + A_2 e^{-\frac{(t-t_2)^2}{w_2^2}} \quad (3.2)$$

t_1 , t_2 , w_1 , and w_2 are parameters define the Gaussian functions. $k_d(T_s)$ is the temperature-dependent desorption rate constant, and $[CO_{(a)}]_t$ is the number of adsorbed CO molecules. $[CO_{(a)}]_t$ can be solved by the time-dependent flux of incident CO and desorbing molecules below:

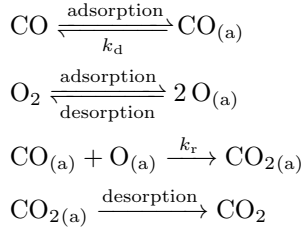
$$\frac{d[CO_{(a)}]}{dt} = \phi_i(t) - k_d(T_s) [CO_{(a)}] \quad (3.3)$$

which can be integrated to give:*

$$\begin{aligned} [CO_{(a)}]_t = e^{-k_d t} \cdot \frac{\sqrt{\pi}}{2} & \left(A_1 e^{k_d t_1 + \frac{k_d^2 w_1^2}{4}} w_1 \text{Erf}\left(\frac{t_1}{w_1} + \frac{k_d w_1}{2}\right) \right. \\ & - A_1 e^{k_d t_1 + \frac{k_d^2 w_1^2}{4}} w_1 \text{Erf}\left(\frac{t}{w_1} - \frac{t_1}{w_1} - \frac{k_d w_1}{2}\right) \\ & + A_2 e^{k_d t_2 + \frac{k_d^2 w_2^2}{4}} w_2 \text{Erf}\left(\frac{t_2}{w_2} + \frac{k_d w_2}{2}\right) \\ & \left. - A_2 e^{k_d t_2 + \frac{k_d^2 w_2^2}{4}} w_2 \text{Erf}\left(\frac{t}{w_2} - \frac{t_2}{w_2} - \frac{k_d w_2}{2}\right) \right) \quad (3.4) \end{aligned}$$

3.4.2. CO oxidation

The simplest kinetic model for CO oxidation via Langmuir-Hinshelwood (L-H) mechanism as follows:



With the following assumptions: (1) no oxygen desorption under CO oxidation reaction temperature; (2) CO_2 immediately desorbs from the surface after reaction. The CO_2 production rate is:

$$\frac{d[CO_2]}{dt} = k_r [O_{(a)}] [CO_{(a)}]_t \quad (3.5)$$

*This equation is solved using Mathematica with the initial condition $[CO_{(a)}](t=0) = 0$.

Where k_r is the reaction rate constant, and $[O_{(a)}]$ is the number of adsorbed O-atoms.

Since the oxygen flux to the surface is much larger than the CO flux, we assumed that the number of O-atoms on the surface, $[O_{(a)}]$, remained constant throughout the reaction, giving pseudo first-order kinetics: $k_{pf}(T_s) = k_r(T_s) [O_{(a)}]$. The CO₂ flux is then described in the following equation:

$$flux(CO_2)(t, T_s) = k_{pf}(T_s) [CO_{(a)}]_t \quad (3.6)$$

$k_{pf}(T_s)$ is the pseudo first-order reaction rate coefficients, and the adsorb CO, $[CO_{(a)}]_t$ can be solved by the time-dependent flux of incident CO, desorbing CO and CO consumption from oxidation, as describes below:

$$\begin{aligned} \frac{d[CO_{(a)}]}{dt} &= \phi_i(t) - [k_d(T_s) + k_{pf}(T_s)] [CO_{(a)}]_t \\ &= \phi_i(t) - k(T_s) [CO_{(a)}]_t \end{aligned} \quad (3.7)$$

$$\begin{aligned} [CO_{(a)}]_t &= e^{-kt} \cdot \frac{\sqrt{\pi}}{2} \left(A_1 e^{kt_1 + \frac{k^2 w_1^2}{4}} w_1 \text{Erf} \left(\frac{t_1}{w_1} + \frac{k w_1}{2} \right) \right. \\ &\quad - A_1 e^{kt_1 + \frac{k^2 w_1^2}{4}} w_1 \text{Erf} \left(\frac{t}{w_1} - \frac{t_1}{w_1} - \frac{k w_1}{2} \right) \\ &\quad + A_2 e^{kt_2 + \frac{k^2 w_2^2}{4}} w_2 \text{Erf} \left(\frac{t_2}{w_2} + \frac{k w_2}{2} \right) \\ &\quad \left. - A_2 e^{kt_2 + \frac{k^2 w_2^2}{4}} w_2 \text{Erf} \left(\frac{t}{w_2} - \frac{t_2}{w_2} - \frac{k w_2}{2} \right) \right) \end{aligned} \quad (3.8)$$

Results and Discussion

This chapter summarizes the results presented in PART II. For a detailed account of the results, the reader is referred to **Papers 1–3**. Alternatively, a summary of the key results from these investigations will be presented in Chapter 5.

4.1. NAP-VMI calibration and performance under NAP

4.1.1. VMI simulation

Figure 4.1 shows the electric field and ion trajectory simulation with COMSOL Multiphysics. The ions with a mass-to-charge ratio, $m/z=28$ and kinetic energy, $E_k=0.03, 0.27, 0.75$ eV are released from the midpoint of the R and E1 electrodes and 0.5 and 1 mm along the laser propagation direction. Eight equal spaced directions parallel to the detector are considered. Due to the elevated gas pressure in the scattering chamber, the applied voltages in this chamber are set low (< 500 V) to avoid an electrical breakdown. The simulated voltages are: R=500 V, E1=480 V, E2=400 V, G=0 V, F1=-3000 V, F2=-1500 V, F3=0 V, F4=-1500 V. The ion optics can operate using only R, E1, and G electrodes, like the traditional VMI setting (Eppink & Parker 1997) with (R=1000 V, E1=720 V, E2=0 V, G=0 V, F1=0 V, F2=0 V, F3=0 V, and F4 = 0 V). The ions can pass through the 3 mm aperture due to the compact design. Similar to the design presented by Long *et al.* for liquid microjet photoelectron imaging (Long *et al.* 2021).

4.1.2. VMI calibration and performance

For testing the VMI and speed calibration, we used N_2O photodissociation (the details are described in Section 3.3.1). The speed calibration of VMI was done using the DC sliced image of N_2 fragments ($J=74$) from N_2O photodissociation, since we know the N_2 recoil speed, yielding a value of 11.5 m/s per pixel. Figure 4.2 shows (a) the VMIs of N_2 fragments from N_2O photodissociation at various J states along with (b) a plot comparing the experimental values and the calculated values (Nishide & Suzuki 2004; Kawamata *et al.* 2006). Our measured values agree with the previous work. These images show that the ion optics can properly map the full velocity distribution, as long as the particles get to the center.

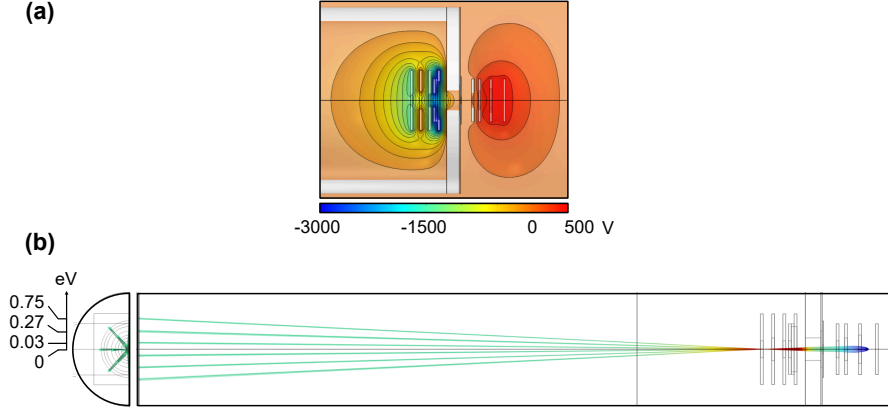


Figure 4.1: Simulation of (a) the electric field and (b) ion trajectories.

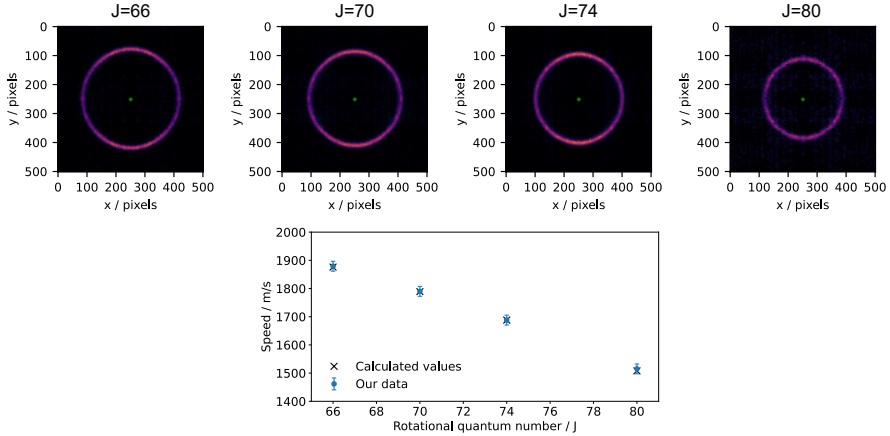


Figure 4.2: Comparison of VMIs of N_2 fragments ($J=66$, 70 , 74 , and 80) from N_2O photodissociation and a plot comparing the experimental values and the calculated values.

4.1.3. VMI performance under NAP

NAP-VMI can operate at pressure in the scattering chamber up to 10^{-3} mbar. Figure 4.3 shows the DC sliced velocity map images of N_2 ($J = 74$) fragments from N_2O dissociation under high vacuum (left panel: 5×10^{-9} mbar) and near-ambient pressure (right panel: 1×10^{-3} mbar of Argon) with their speed and angular distribution. Collisions with the background Ar reduced the total

signal and broadened the speed distribution (by factors around 3 in this case) at near-ambient pressure, which is normal for (N)AP experiments, but the dynamical information is still visible.

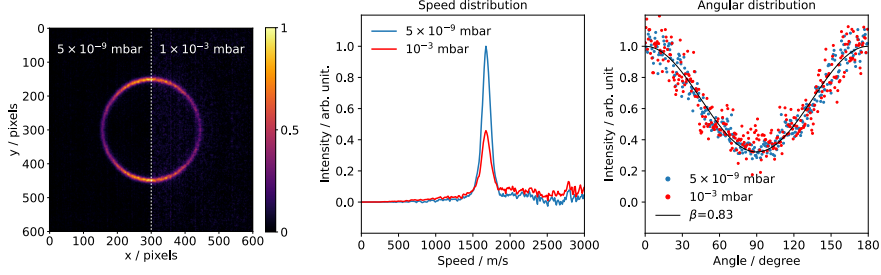


Figure 4.3: VMIs of N_2 ($J = 74$) fragments from N_2O dissociation (left panel: 5×10^{-9} mbar; right panel: 1×10^{-3} mbar of Argon) and their corresponding speed and angular distribution.

Figure 4.4 shows the velocity map images of N_2 scattering on Pd(110) under high vacuum (left panel: 5×10^{-9} mbar) and near-ambient pressure (right panel: 1×10^{-3} mbar in Argon) with their speed and angular distribution. No significant difference is found, comparing the speed distribution between high vacuum and near-ambient environment. There is some broadening in angular distribution for scattered N_2 in the near-ambient pressure argon environment, which we attribute to collisions with Ar atoms.

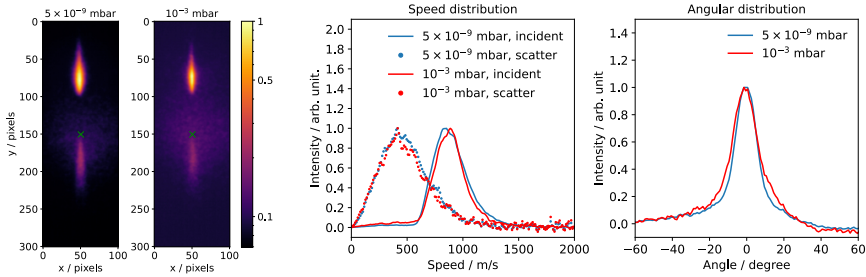


Figure 4.4: VMIs of N_2 scattering on Pd(110) (left panel: 5×10^{-9} mbar; right panel: 1×10^{-3} mbar in Argon) and their corresponding speed and angular distribution.

4.2. CO scattering and oxidation on Pd(110)

CO oxidation on metal catalysts is a simple model system to study catalytic reaction mechanism. In this section, we study the CO oxidation on the Pd(110) surface with NAP-VMI.

4.2.1. CO scattering

Figure 4.5(a) shows the typical CO scattering VMI on the clean Pd(110) surface at surface temperature, $T_s = 650$ K. Figure 4.5(b) shows the corresponding speed distribution of the CO scattered molecules. Figure 4.5(c) shows the time-resolved measurement (blue dots) of CO scattering on Pd(110) at various surface temperatures ($T_s = 610$ – 670 K); data are selected in the area below the center of a 20-degree sector spanning 40–60 pixels. The CO scattering flux can be described with the kinetic model equation (3.1). We fit this kinetic model (red curves) to the experimental kinetic traces to determine the desorption rate constants of CO on Pd(110) for the known surface temperatures. Figure 4.5(d) shows the Arrhenius plot of the rate constants for CO trapping desorption. From this, we determine a desorption activation energy of (1.17 ± 0.03) (eV) and a prefactor of $(0.43 \pm 0.41) \times 10^{13} \text{ s}^{-1}$. Jones *et al.* report a desorption activation energy of 1.27–1.37 eV (Jones *et al.* 1999). In their study, the desorption activation energy was acquired by the TPD method, and the activation energy was calculated from Readhead analysis (Readhead 1962) with an assumed prefactor of $5 \times 10^{13} \text{ s}^{-1}$. In our experiment, we also measured a lower desorption activation energy and prefactor, suggesting that the TPD method with the assumed prefactor overestimates the activation energy.

4.2.2. CO oxidation

Figure 4.6 (a) shows a typical VMI of CO_2 from CO oxidation on Pd(110) surface at $p_{\text{O}_2} = 8 \times 10^{-8}$ mbar and $T_s = 650$ K. Figure 4.6(b) shows the corresponding speed distribution of the CO_2 products. The speed distribution consists of two components, one slow and one fast. Figure 4.6(c) shows the time-resolved measurement of CO_2 from CO oxidation on Pd(110) surface at $p_{\text{O}_2} = 8 \times 10^{-8}$ mbar and $T_s = 550$ – 625 K for both slow (blue dots, data are selected in the area below the center of a 20-degree sector spanning 20–50 pixels) and fast (red dots, data are selected in the area below the center of a 20-degree sector spanning 120–180 pixels) components. The kinetic traces for both components are almost identical. The individual kinetic model of the CO_2 flux for both components can be described with the equation (3.6). We fit this kinetic model (red curves for the fast component and blue curves for the slow component) to the experimental kinetic traces to determine the pseudo first-order reaction coefficient of CO oxidation on Pd(110). Figure 4.6(d) shows the Arrhenius plot of the pseudo first-order reaction rate coefficients for CO oxidation on Pd(110). The oxidation activation energies for both components are around (1.0 ± 0.13) eV. Based on our experimental data, kinetic modeling, and previous studies on Pd(110) (Section 2.5), we propose a mechanism for CO oxidation on Pd(110).

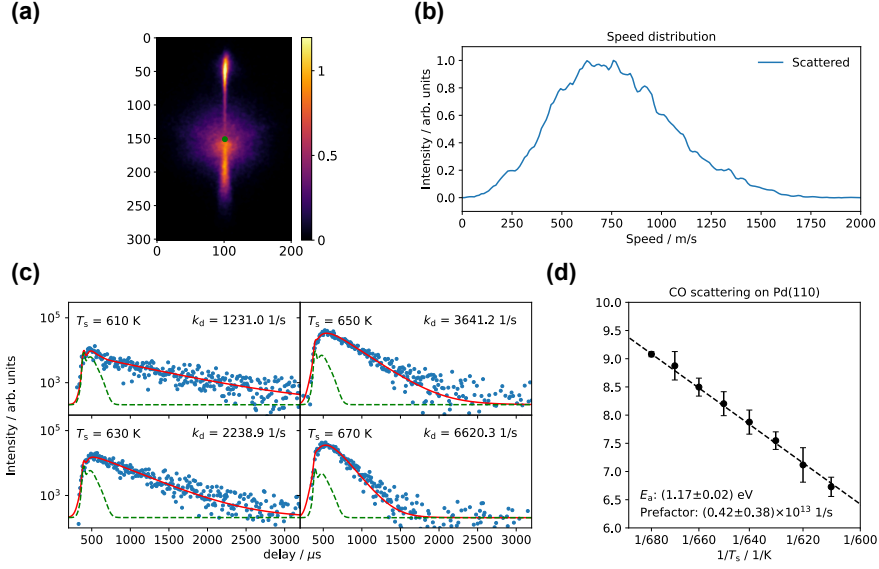
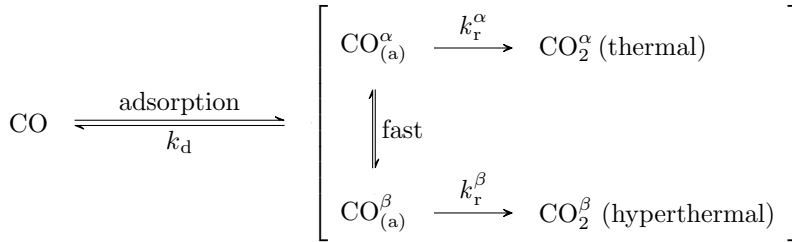


Figure 4.5: (a) VMI of CO scattering on Pd(110) at $T_s = 650$ K; (b) corresponding scattered CO speed distribution in (a); (c) kinetic trace of CO scattering at $T_s = 610$ – 670 K; (d) Arrhenius plot of the rate constants for CO trapping desorption derived in (c).

The mechanism involves two types of fast and interchangeable CO adsorption sites (ridge and trough sites) that react with a single type of oxygen adatom. CO from two different adsorption sites approaches the oxygen adatom, leading to two reaction channels, and results in two CO_2 products: thermal (slow in speed) and hyperthermal (fast in speed), as shown in figure 4.7.

The reaction mechanism is described as follow:



The time dependence of the two channels is mixed if the CO can interchange quickly on the experimental time scale. Therefore, what we derive are the effective pseudo first-order oxidation rate coefficients, $k_{\text{pf}}^{\text{eff}}(T_s) = k_{\text{pf}}^{\alpha} + k_{\text{pf}}^{\beta}$.

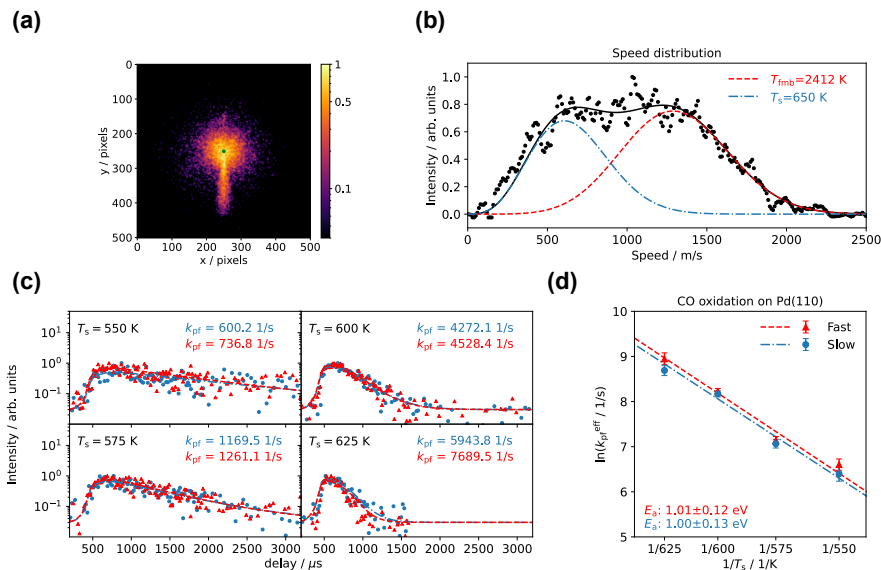


Figure 4.6: (a) VMI of CO₂ production of CO on Pd(110) at $T_s = 650$ K and $p_{O_2} = 7.5 \times 10^{-8}$ mbar; (b) corresponding CO₂ speed distribution in (a); (c) kinetic trace of CO₂ production at $T_s = 550$ – 625 K and $p_{O_2} = 7.5 \times 10^{-8}$ mbar; (d) Arrhenius plot of the pseudo first-order reaction rate coefficients for CO oxidation on Pd(100) derived in (c).

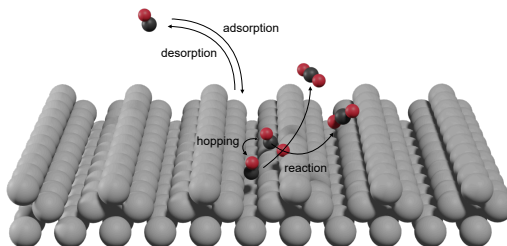


Figure 4.7: Schematic diagram of the CO oxidation on Pd(110)-missing row structure.

4.2.3. CO oxidation under oxygen rich environments

Figure 4.8(a) shows the CO₂ apparent reaction coefficient (left) and related total CO₂ signals (right) under $p_{O_2} = 2.5 \times 10^{-8}$ mbar to 1×10^{-6} mbar. On the top of

the panel, the corresponding surface structure from ref. (Westerström *et al.* 2009) are labeled. The apparent reaction coefficients combine the CO_2 signals from both fast and slow channels. It increases with p_{O_2} until $p_{\text{O}_2} = 5 \times 10^{-7}$ mbar, at which point the reaction happens so fast and reaches the time resolution limit of our current setup. The CO_2 signal increases with p_{O_2} until $p_{\text{O}_2} = 5 \times 10^{-8}$ mbar and decreases with further increase of p_{O_2} . At $p_{\text{O}_2} > 5 \times 10^{-7}$, almost no CO_2 production happens. Figure 4.8(b) shows the speed distribution of CO_2 at $T_s = 650$ K and $p_{\text{O}_2} = 5 \times 10^{-6}$ mbar, where the CO_2 production is highly suppressed. It shows that the slow component almost disappears under this reaction condition. According to ref. (Westerström *et al.* 2009), the trough sites also disappear at 1×10^{-6} mbar due to the surface reconstruction from the $\text{c}(2 \times 4)\text{-O}$ missing row structure to the complex surface oxide structures. Therefore, we assign the slow component to the CO adsorption on the troughs of the $\text{Pd}(110)\text{--}(1 \times 2)$ missing row structure, and the fast channel can result from CO adsorption on the ridges of the $\text{Pd}(110)\text{--}(1 \times 2)$ missing row structure or the defect sites on the complex surface oxide, both on the top layer of $\text{O}/\text{Pd}(110)$. Figure 4.8(c) and (d) show the VMIs and the kinetic traces of CO scattering on the clean $\text{Pd}(110)$ and at $p_{\text{O}_2} = 5 \times 10^{-6}$ mbar, which correspond to the surface oxide structure. The VMIs show that the CO scattering signal is far stronger on the surface oxide than on the clean surface. The kinetic traces show that the resident time of the CO is shorter on the oxide surface than on the clean surface. The results of CO scattering imply that CO molecules do not stick to or adsorb well on the oxide surface, leading to low CO_2 production.

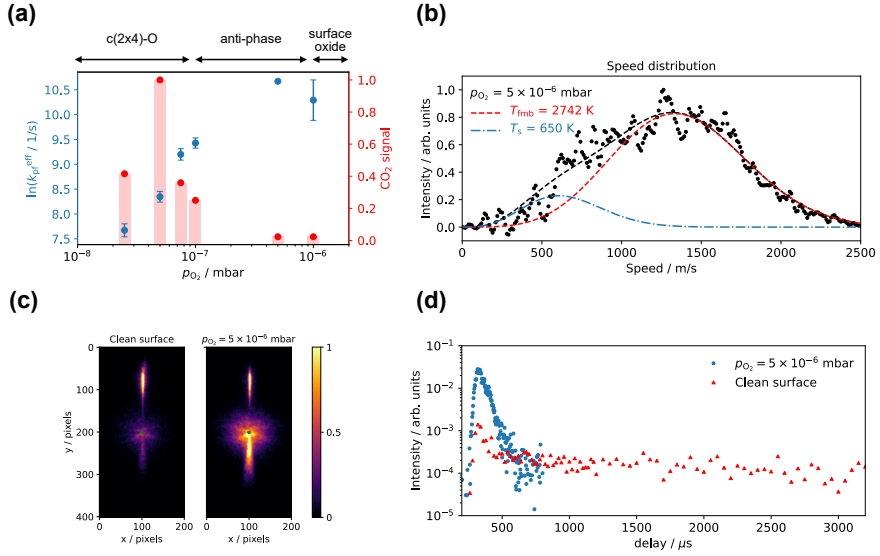


Figure 4.8: (a) Plots of the apparent CO reaction rate and total CO_2 signals with various p_{O_2} ; (b) CO_2 speed distribution of CO oxidation on Pd(100) at $T_s = 650 \text{ K}$ and $p_{\text{O}_2} = 5 \times 10^{-6} \text{ mbar}$; (c) VMIs of CO scattering on Pd(110) on the clean Pd(110) and at $p_{\text{O}_2} = 5 \times 10^{-6} \text{ mbar}$ in the scattering chamber; (d) corresponding kinetic traces from (c).

4.3. CO scattering and oxidation on Pd(100)

CO oxidation on Pd(100) draws more attention than on Pd(110) due to the formation of multiple oxide structures, which can function as active phases for CO oxidation. Despite extensive research, there are still questions about surface structures and active phases. In this section, we study the CO oxidation on the Pd(100) surface with NAP-VMI.

4.3.1. CO scattering

CO scattering is studied to derive the desorption coefficients, k_d , which is essential for the kinetic modeling of CO oxidation. Figure 4.9(a) shows the comparison of the CO desorption kinetic traces of CO scattering on Pd(100) surface with no oxygen (clean surface) and with $p_{O_2} = 5 \times 10^{-8}$ mbar in the scattering chamber (we estimate a $O_2/CO = 5/1$ from their flux). The residence time of CO on the partially oxidized surface is much longer than on the clean surface, suggesting that the CO desorption activation energy increases. Due to the lack of details of the surface under reaction conditions, such as the surface structures, CO adsorption sites, and reaction mechanisms, we cannot derive the desorption rate coefficients from the kinetic traces; instead, the apparent desorption rate coefficients are derived from the kinetic model of the CO scattering flux with the equation (3.1).

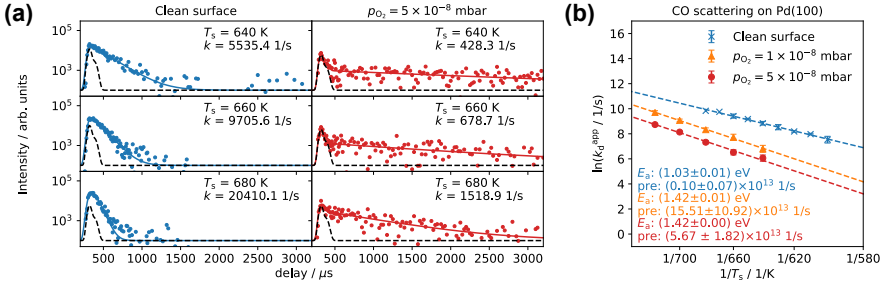


Figure 4.9: (a) Comparison of the kinetic traces (data are selected in the area below the center of a 20-degree sector spanning 50–70 pixels) of CO scattering on clean Pd(100) and with $p_{O_2} = 5 \times 10^{-8}$ mbar in scattering chamber (blue/red curves show the fit of the scattering model; black dash curve represent the direct scattering component); (b) Arrhenius plot of the apparent desorption rate coefficients for CO trapping desorption derived in (a) and at $p_{O_2} = 1 \times 10^{-8}$ mbar.

Figure 4.9(b) shows the Arrhenius plot of the apparent desorption rate coefficients for CO trapping desorption on Pd(100) with various p_{O_2} in the scattering chamber. We determine a desorption activation energy of (1.05 ± 0.01) eV and a prefactor of $(0.13 \pm 0.12) \times 10^{13} s^{-1}$ on the clean Pd(100). We introduced

oxygen to $p_{\text{O}_2} = 1 \times 10^{-8}$ and 5×10^{-8} mbar in the scattering chamber, and we derived a higher apparent desorption activation energy around 1.42 eV; however, the cause of this observation remains to be explained. Gao *et al.* observed new CO vibration modes (2142 and 2087 cm^{-1}) on the Pd(100) surface by PM-IRAS under an oxygen rich environment ($\text{O}_2/\text{CO} > 5/1$), which they ascribe to the adsorption associated with oxygen species (Gao *et al.* 2009a). Mehar *et al.* studied CO adsorption on multilayer and single layer PdO with RAIRS, suggesting an atop-CO adsorption (2144 cm^{-1}) on these oxide surfaces (Mehar *et al.* 2018). The change in apparent desorption activation energy may be due to the formation of oxide surfaces and CO molecules preferentially desorb from these sites.

4.3.2. CO oxidation

Figure 4.10(a) shows the CO_2 production VMI at $T_s = 510$ K and $p_{\text{O}_2} = 1 \times 10^{-6}$ mbar in the scattering chamber. Figure 4.10(b) shows the corresponding speed distribution, and the mean energy of the CO_2 was expressed in temperature, $T_{\text{fmb}} = 1638$ K. The speed distribution shows a single peak for all the pressure and temperature ranges in our experiments, unlike Pd(110), which shows two speed distributions (see Section 4.2.2). Moula *et al.* (Moula *et al.* 2000) reported the velocity distribution of the desorbing product CO_2 in CO oxidation on Pd(100), with $T = 1600$ K, which is in agreement with our VMI experiment.

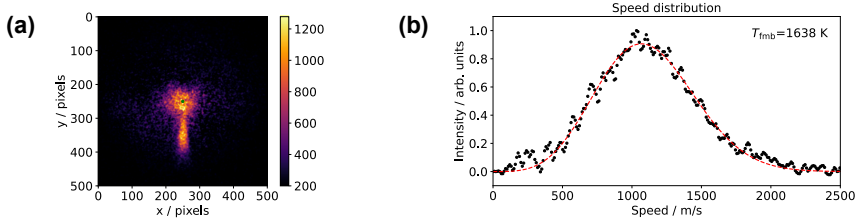


Figure 4.10: (a) Velocity map image of product CO_2 . Image was acquired at surface temperature of 510 K and $P_{\text{O}_2} = 1 \times 10^{-6}$ mbar (scanning molecular beam–laser delay from 200–3200 μs). (b) The speed distribution of CO_2 products in (a). Signal was corrected by removing the background build up CO_2 signal and integrated 20-degree sector below the center of image (greed dot). The red dashed curve is the fitting from flowing Maxwell-boltzmann distribution.

Figure 4.11(a) shows the plot of total CO_2 production signals to oxygen pressure in the scattering chamber at different surface temperatures (data are collected from scanning molecular beam–laser delay from 200–3200 μs , which includes the the entire oxidation process). At high surface temperatures ($T_s > 600$ K), the CO_2 production first increases with oxygen pressure and reaches a maximum around $p_{\text{O}_2} = 2 \times 10^{-7}$ mbar, and with further increase in oxygen pressure the CO_2 production decreases. At low temperatures ($T_s < 600$

K), the CO_2 production exhibit two local maxima around $p_{\text{O}_2} = 1 \times 10^{-7}$ and $p_{\text{O}_2} = 1 \times 10^{-6}$ mbar. In a recent report (Mehar *et al.* 2023), Mehar *et al.* observed the temperature dependent growth of PdO during the oxidation of Pd(100). At low temperatures, Pd(100) forms a thin multilayer PdO(101) structure; at high temperatures, Pd(100) forms a mixture of a thin multilayer PdO(101) and a thicker multilayer PdO(100). The multilayer PdO(100) has low activity toward CO oxidation due to the lack of coordinatively unsaturated Pd sites for CO adsorption. Figure 4.11(a) shows that at $p_{\text{O}_2} = 1 \times 10^{-6}$ mbar, higher surface temperatures reduce the CO_2 production. Therefore we suggest that the surface forms the multilayer PdO(101) and PdO(100) at this pressure. At a lower oxygen pressure, $p_{\text{O}_2} = 1 \times 10^{-7}$ mbar, we suggest that the surface forms a $(\sqrt{5} \times \sqrt{5})$ -O single layer surface oxide, which is the most common structure during CO oxidation. The CO_2 production decreases from $p_{\text{O}_2} = 1 \times 10^{-7}$ mbar to $p_{\text{O}_2} = 1 \times 10^{-6}$ mbar, which might be due to the growth of the $(\sqrt{5} \times \sqrt{5})$ -O single layer surface oxide, which is less active for CO oxidation compared to the multilayer PdO(101) based on the TPD/TPRS study by Mehar *et al.* (Mehar *et al.* 2018).

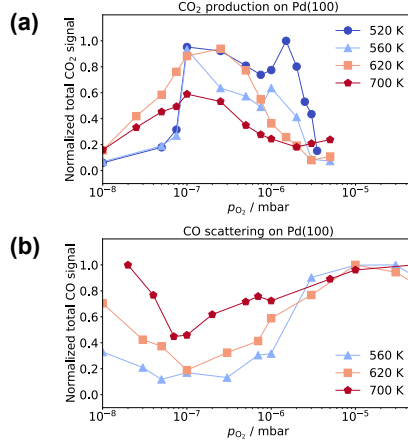


Figure 4.11: (a) Plots of the normalized total CO_2 production signals and (b) normalized total CO scattering signals with various p_{O_2} .

Figure 4.11(b) shows the plot of total CO scattering signals to oxygen pressure in the scattering chamber at various surface temperatures. The results show that once $p_{\text{O}_2} \geq 1 \times 10^{-6}$ mbar, the sticking of CO on Pd(100) decreases, leading to low CO_2 production. It also implies that CO oxidation follows the L-H mechanism instead of the MvK mechanism (Mars & van Krevelen 1954), which involves oxygen atoms in the surface oxide lattice for CO oxidation.

In the following sections, we focus on CO oxidation at $p_{\text{O}_2} = 1 \times 10^{-6}$ and $p_{\text{O}_2} = 1 \times 10^{-7}$ mbar in the scattering chamber, which represent CO oxidation on different O/Pd(100) metastable structures.

4.3.3. CO oxidation: $p_{\text{O}_2} = 1 \times 10^{-6}$ mbar

CO oxidation on Pd(100) is sensitive to the history of surface preparation (Zheng & Altman 2002b). In our experiment, the CO_2 kinetic traces vary depending on whether the experiment starts at (1) a high temperature (560 K) or (2) a low temperature (460 K). The data was taken 10 minutes after the surface reached the set temperature, with the molecular beam running to make sure the surface reached its steady state. Figure 4.12(a) shows the kinetic traces of CO oxidation on Pd(100) at $p_{\text{O}_2} = 1 \times 10^{-6}$ mbar and at the same three temperatures but with different treatment histories. The left panels show the one that started at the high temperature; the right panels show the one that started at the low temperature. The surface with the high temperature history shows single exponential decay. The surface with the low temperature history is not well described with a single exponential decay; instead, it shows, at least, a biexponential decay. The biexponential kinetic trace implies two channel reaction. The two reaction channels may be due to the fact that reactions happen on two different metastable structures. A previous report (Goodwin *et al.* 2021) showed that the oxide layer and Pd metal coexist even under oxygen rich environment ($\text{O}_2/\text{CO} = 50/4$).

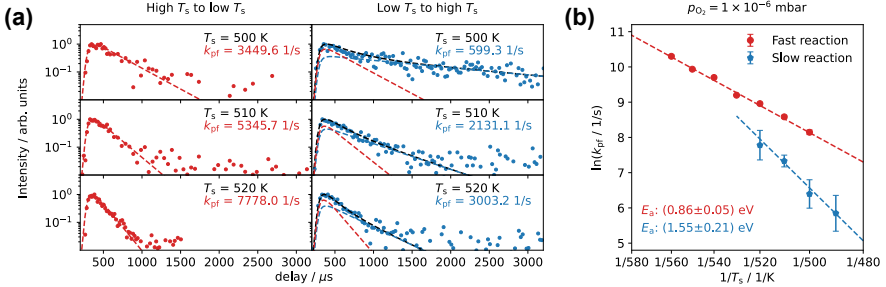


Figure 4.12: (a) Comparison of the kinetic traces of CO oxidation on Pd(100) and with $p_{\text{O}_2} = 1 \times 10^{-6}$ mbar in scattering chamber; (b) Arrhenius plot of the rate coefficients for CO_2 production derived in (a).

The kinetic model of the CO_2 flux for single exponential decay can be described with the equation (3.6). We fit this kinetic model to the experimental kinetic traces to determine the pseudo first-order reaction coefficients of CO oxidation on Pd(100). For the biexponential decay, we assume two active phases (metal and oxide) coexist and both reaction channels follow L-H mechanism, giving the modified equation by adding a second reaction component as in the

equation below:

$$\begin{aligned} flux(CO_2)(t, T_s) = & A_{\text{metal}} \cdot k_{\text{pf}}^{\text{metal}}(T_s) [CO_{(a)}^{\text{metal}}]_t \\ & + A_{\text{oxide}} \cdot k_{\text{pf}}^{\text{oxide}}(T_s) [CO_{(a)}^{\text{oxide}}]_t \end{aligned} \quad (4.1)$$

where

$$[CO_{(a)}^i]_t \propto e^{(k_d^i + k_{\text{pf}}^i)t} \quad (4.2)$$

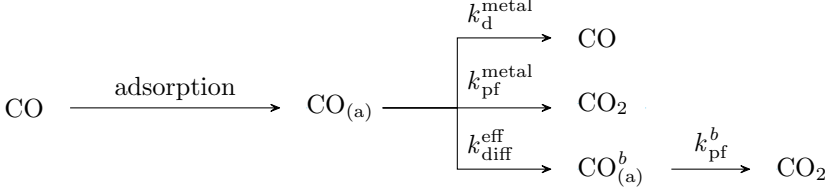
The factors A_{metal} and A_{oxide} are used to scale the model to the signal in the experiment. Under reaction temperatures, the desorption rate coefficients (k_d^i) determined in the previous section (Section 4.3.1) are so small compared to the reaction rate coefficients, that we assume we can neglect them. Hence the reaction coefficients, $k = k_d^i + k_{\text{pf}}^i$, determined from the kinetic traces can be represented as reaction rate, k_{pf}^i . The second rate constant was obtained by fitting with a known first rate coefficient from the single exponential experiments. We refer to the rate coefficient in the single exponential decay as the fast channel (red curve) and the second rate coefficient in the biexponential decay as the slow channel (blue curve).

Figure 4.12(b) shows the Arrhenius plot of the pseudo first-order reaction rate coefficients for CO oxidation on Pd(100). The oxidation activation energies for the fast and slow channels are $E_a = (0.86 \pm 0.05)$ and (1.55 ± 0.21) eV, respectively. In our experiments, we observe increases in CO_2 production at high temperatures, which seems to contradict the results we show in figure 4.11, since high temperatures reduce the CO_2 production due to the growth of Pd(100) multilayer oxide. However, the reaction temperature is still too low (< 600 K) for the formation of PdO(100) multilayer oxide. Therefore, we attribute the fast channel to CO oxidation on the Pd (100) metal surface and the slow channel to multilayer PdO(101), since surface oxide cannot develop at high temperatures due to prompt O consumption from rapid CO oxidation. Additionally, the apparent desorption activation energy derived from O/Pd(100) k_d^{app} is within the range of reaction activation energy of the slow channel, also suggesting that this reaction channel is associated with O/Pd(100).

4.3.4. CO oxidation: $p_{O_2} = 1 \times 10^{-7}$ mbar

The kinetic traces of CO oxidation on Pd(100) at $p_{O_2} = 1 \times 10^{-7}$ mbar show similar behavior to $p_{O_2} = 1 \times 10^{-6}$ mbar. We expected the surface to be $(\sqrt{5} \times \sqrt{5})$ -O single layer surface oxide. We could fit the kinetic traces with equation (4.1), assuming the single layer oxide as another active phase for CO oxidation. Although previous reports have shown that $(\sqrt{5} \times \sqrt{5})$ -O single layer surface oxide is inactive to CO oxidation due to its inability to adsorb CO molecules (Gao *et al.* 2008; Mehar *et al.* 2018). We propose a different reaction model inspired by the reduction of Pd surface oxide by CO (Fernandes *et al.* 2014; Hoffmann *et al.* 2015). CO molecules diffuse to the domain boundary of the surface oxide and react with the surface oxide to produce CO_2 . The

reaction mechanism is described as follow:



The CO molecules adsorb on the Pd(100) surface, $\text{CO}_{(a)}$, can desorb into the gas phase, react to surface O-atoms, and diffuse to the domain boundary of the $(\sqrt{5} \times \sqrt{5})\text{-O}$ single layer surface oxide and later react. The CO_2 flux is then described as follow:

$$\text{flux}(\text{CO}_2) \propto \underbrace{k_{\text{pf}}^{\text{metal}} [\text{CO}_{(a)}]_0 \cdot e^{-(k_d^{\text{metal}} + k_{\text{pf}}^{\text{metal}} + k_{\text{diff}}^{\text{eff}})t}}_{\text{fast}} + \underbrace{k_{\text{diff}}^{\text{eff}} k_{\text{pf}}^b [\text{CO}_{(a)}^b]_0 \cdot e^{-k_{\text{pf}}^b t}}_{\text{slow}} \quad (4.3)$$

Where $k_{\text{diff}}^{\text{eff}}$ is the effect diffusion rate coefficient, which includes the diffusion rate and the number of adsorption sites at the boundary; k_{pf}^b is the CO pseudo first-order oxidation rate at the boundary; and $\text{CO}_{(a)}^b$ is the number of CO molecules that adsorb at the boundary.

4.13(a) show the kinetic traces of CO oxidation on Pd(100) at $p_{\text{O}_2} = 1 \times 10^{-7}$ mbar in the scattering chamber and with same temperatures but with different treatment histories, same as before. We expect the surface with the high temperature history to be a metal surface and the surface with the low temperature history to be partially metal and partially single layer surface oxide, for the same reason as we mentioned in Section 4.3.3, that surface oxide cannot develop at high temperatures due to rapid O consumption from fast CO oxidation. We fitted the kinetic traces with equation (4.3) and determined $k_{\text{pf}}^{\text{metal}}$ and k_{pf}^b .

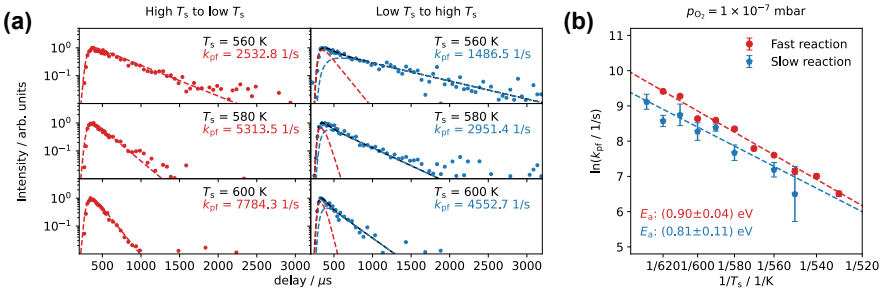
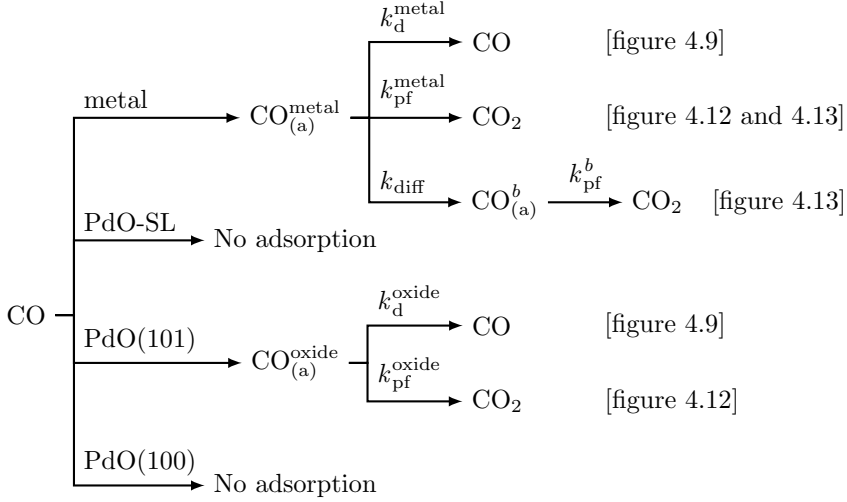


Figure 4.13: (a) Comparison of the kinetic traces of CO oxidation on Pd(100) and with $p_{\text{O}_2} = 1 \times 10^{-7}$ mbar in scattering chamber; (b) Arrhenius plot of the rate coefficients for CO_2 production derived in (a).

Figure 4.13(b) shows the Arrhenius plot of the pseudo first-order reaction rate coefficients for CO oxidation on Pd(100). The oxidation activation energies on the metal and at the boundary are $E_a = (0.90 \pm 0.04)$ and (0.81 ± 0.11) eV, respectively. Additionally, the oxidation activation energies for the fast channel in figure 4.12(b) and figure 4.13(b) are very similar, which also suggests that it is a reaction on a common surface, which we attribute to the Pd(100) metal surface.

For a better understanding of the results, the following chart summarizes the reaction scheme in this section.



Pd(100) exhibits four surface structures (Pd(100) metal phase, PdO(101) single layer, PdO(101) multilayer, and PdO(100) multilayer) during CO oxidation. Among them, the Pd(100) metal phase and the PdO(101) multilayer are active to CO oxidation. In addition, CO₂ can be produced through reduction of Pd(100) single layer oxide at the domain boundary. At $p_{O_2} = 1 \times 10^{-6}$ mbar, the surface is dominated by the Pd(100) metal phase and the PdO(101) multilayer. Two pseudo first-order reaction rate coefficients, k_{pf}^{metal} and k_{pf}^{oxide} , are obtained from the time-resolved experiments (figure 4.12). At $p_{O_2} = 1 \times 10^{-7}$ mbar, the surface is dominated by the Pd(100) metal phase and the PdO(101) single layer; as a result, k_{pf}^{metal} and k_{pf}^b are obtained (figure 4.13).

Conclusions and outlook

5.1. Summary and conclusions

The present work demonstrates the design and construction of near-ambient pressure velocity map imaging and its application in catalysis studies. The first section of the thesis focuses on the construction of NAP-VMI and the in depth experimental methodologies. The second section focuses on the study of CO scattering and oxidation reactions on the palladium model surface under oxygen rich environment. We examined two kinds of palladium surfaces: Pd(110) and Pd(100). The main conclusions for this initial part are as follows:

Paper 1 (Chien *et al.* 2022):

- We demonstrated a new VMI setup. With the combination of differential pumping and molecular beam, we are able to study the surface reaction at elevated pressure that drives the surface reconstruction and have a time resolution in μs scale.
- With the current ion optics setting, we are able to reach pressures up to 1×10^{-3} mbar.
- In addition, the concept of NAP-VMI can also be applied to other studies, such as liquid jet photoelectron spectroscopy or molecular beam scattering from liquid surfaces (gas-liquid interaction).

Paper 2 (Submitted to Faraday Discuss.):

- CO₂ VMI shows that there are two reaction channels to CO oxidation on Pd(110) surface: thermal and hyperthermal channels.
- We propose a reaction scheme in which CO reacts to O-atom from two quickly interchangeable CO adsorption sites: one on the troughs of the Pd(110)-(1 \times 2) missing row structure and one on the ridges of the Pd(110)-(1 \times 2) missing row structure or the defect sites on the complex surface oxide, both on the.
- CO₂ production decreases at oxygen rich Pd(110) due to the decrease of CO sticking or adsorption on O/Pd(110), leading to low CO oxidation activity on Pd(110)-surface oxide.

Paper 3 (Manuscript under preparation):

- The CO residence time is longer on the O/Pd(110) surface than on the clean Pd(100) surface. This might be due to the increase in CO desorption and/or CO oxidation activation energy on O/Pd(100).
- We attribute the surface structure during CO oxidation to partially metal and $(\sqrt{5} \times \sqrt{5})$ -O single layer surface oxide at $p_{\text{O}_2} = 1 \times 10^{-7}$ mbar in the scattering chamber; partially metal, multilayer PdO(101) and, PdO(100) at $p_{\text{O}_2} = 1 \times 10^{-6}$ mbar in the scattering chamber.
- The time-resolved experiments show, at least, biexponential feature implying that the coexistence of multiple active phases on Pd(100) during CO oxidation. We developed two reaction models to describe the bimodel activity.
- CO₂ production is suppressed on the highly oxidized PdO surface.

5.2. Future work

Despite the contributions made throughout this thesis, further research is needed to advance knowledge of surface science.

Some ideas for upgrading the machine:

- Increase the angular distribution for the scattering experiment: In Section 3.3.2, we estimate that only molecules within $\pm 15^\circ$ of the scattering plane parallel to the electrodes will be ionized. One possibility for increasing the angular distribution is to optimize the size of the ion optics to maximize the angular acceptance, but this would not be a significant increase. Another approach is to rotate the VMI optics along with the sample surface normal, which increases a lot in the angular acceptance but loses the key feature of VMI, which can acquire the entire angular distribution in a single measurement.
- Increase the sample heating limitation: In Section 3.1.6, the sample holder heating limit is 1000 K due to the working temperature of the sample plate receiver, and we have reached the maximum output of the power supply. It restricts the kind of surfaces we can anneal, such as a platinum surface. We can raise the sample heating limit by changing the power supply and the sample plate receiver material to tantalum or titanium.
- An isolated sample temperature measurement: In Section 3.1.6, the sample holder can apply a potential of up to 500 V to reduce the influence of the electric field from the surface, which is insignificant if the distance between the surface and the ionization center is far (> 15 mm). It can be useful if we need a shorter surface to ionization center distance, which can also increase the angular acceptance. However, due to safety issues, the sample potential and thermocouple should not be used at the same time. An isolated sample temperature measurement can solve this problem.
- A “seal” between the scattering chamber and the preparation chamber: In the initial design, a special seal was designed between the scattering

chamber and the preparation chamber to separate the two chambers during scattering experiments while the sample manipulator could move freely around the VMI ion optics. The parts were made but never installed. It was designed to decrease volume in high pressure experiments and reduce gas consumption.

- A load lock chamber for quick sample exchange.

Research work in the context of this thesis that is possible for future studies is detailed in the following:

- CO scattering on O/Pd(110): In **Paper 2**, we perform CO scattering on the clean Pd(110) surface. CO scattering on O/Pd(110) was examined only to compare the total CO scattering signals with clean surface. The result shows that CO scatter more on the O/Pd(110) surface than the Pd(110) and the CO resident time on O/Pd(110) is shorter than the time resolution of our current setup. Further studies are need to to determine if this is due to a reduction in the CO sticking probability, leading to direct scattering, or due to a reduction in the CO binding energy, leading to faster desorption.
- CO scattering on O/Pd(100): In **Paper 3**, we perform CO scattering on the clean Pd(100) surface. CO scattering on O/Pd(110) was examined only under low oxygen pressure (up to 5×10^{-8} mbar). Further increase in pressure in mid range (1×10^{-7} – 1×10^{-6} mbar), the CO scattering signals are suppressed due to CO oxidation reaction. At higher oxygen pressure ($> 1 \times 10^{-5}$ mbar), the CO scattering signal increases again. CO oxydation on Pd(100) is more complicated due to the growth of PdO, which have multiple structures. Further studies are needed to to determine the sticking probability and binding energy to different PdO structures.
- NAP-VMI is only able to detect molecules leaving the surface, we are lacking the information of the surface structure and the adsorption of reactants. In this thesis, that information relies on many results in the literature. A reactor STM is installed to study the surface structures. Several assumptions in the present kinetic models need to be verified, such as the interchangeable CO adsorption sites on Pd(110)-missing row structure, CO adsorption and diffusion on Pd(100) and O/Pd(100) surface. A time-resolved NAP-XPS or time-resolved infrared study will be good to test these assumptions.

Some experiments were done but not present in this thesis:

- Comparison of VMI speed distribution and REMPI spectroscopy of CO scattering on Pd(110) and O/Pd(110). These experiments were designed to study the desorption mechanism of CO on O/Pd(110). Due to the lack of angular information and geometric configuration of the surface. The CO direct scattering direction and CO trapping desorption overlap, which makes the analysis of the speed distribution and REMPI

spectroscopy very difficult. We lack data of sufficient quality to have solid evidence and a conclusion.

- H₂ associative desorption on Pd(110) and S-poisoned Pd(110). The purpose of these experiments are testing ability of detecting the desorbing hydrogen molecules. We are able to ionize hydrogen molecules by 2+1 REMPI through $E, F^1\ ^1\Sigma_g^+ \leftarrow X\ ^1\Sigma_g^+$ transition at wavelengths around 203 nm (Rinnen *et al.* 1991).

5.3. Outlook

For an outlook, I want to emphasize that chemical reactions often present distinct characteristics when observed at the atomic scale. This thesis has demonstrated that, intriguingly, even when using the same Pd catalyst, the reaction mechanisms and surface structures can vary significantly depending on the facets involved. This raises a crucial question: to what extent do these detailed variations contribute to our understanding of reaction behaviors and, more importantly, enhance performance in practical applications? Investigating such details is more than just a theoretical endeavor; this information has the potential to completely change the way we think about catalysis and open the door to more effective and sustainable chemical processes. By gaining an understanding of these variations at the atomic level, we can create catalytic processes that are more effective and efficient, which will progress a range of industrial and environmental applications.

Acknowledgements

The present thesis represents my work as a PhD from November 2018 to February 2024. The entire journey has been incredibly smooth, thanks to support from everyone involved.

I want to start by thanking my main supervisor, Dan. Being your first PhD student and working on such an exciting project has been an amazing experience. Our casual coffee break chats instead of formal meetings were great for brainstorming ideas. You gave me so much freedom in designing the machine and the project I want to work on. I am especially appreciative for the important moments and decisions you made that were essential to our achievement, such as finding the first ion signal and suggesting the magic wavelength for ionizing CO_2 . I am also immensely thankful to Klas, the head of division and my co-supervisor during my doctoral studies. I've had to extend my PhD a few times, and I appreciate all the extra financial support you've provided.

I also participated in the work at the Department of Physics at Stockholm University and the trips to synchrotron facilities for XPS experiments. I would like to thank Henrik Öström and Mats Götelið for welcoming me into these projects.

I would also like to thank my friends. Especially Elise, Lea, and Marc. Elise, your presence has been a source of joy. You've always put in tremendous effort to help me in any way you can. Your honesty and directness, particularly during tough times, have kept me in the right direction. Lea, working with you was fantastic. The laser, software, and models you made were essential, and I've always trusted your decision for the high standards and ethics you have. Marc, thank you for sharing the L^AT_EX template with me. Additionally, I would like to thank Louise for checking the Swedish abstract for me.

Lastly, I want to thank everyone and everything I've encountered over these years. And to you, the reader, I also want to express my gratitude for reading this thesis. Your interest and attention are deeply appreciated, and they mean a lot to me.

Bibliography

- ASHFOLD, M. N. R., NAHLER, N. H., ORR-EWING, A. J., VIEUXMAIRE, O. P. J., TOOMES, R. L., KITSOPOULOS, T. N., GARCIA, I. A., CHESTAKOV, D. A., WU, S.-M. & PARKER, D. H. 2006 Imaging the dynamics of gas phase reactions. *Physical Chemistry Chemical Physics* **8** (1), 26–53.
- BAXTER, R. J. & HU, P. 2002 Insight into why the Langmuir–Hinshelwood mechanism is generally preferred. *The Journal of Chemical Physics* **116** (11), 4379–4381.
- BEHM, R. J., CHRISTMANN, K., ERTL, G. & VAN HOVE, M. A. 1980 Adsorption of CO on Pd(100). *The Journal of Chemical Physics* **73** (6), 2984–2995.
- BERZELIUS, J. 1835 Sur un force jusqu’ici peu remarquée qui est probablement active dans la formation des composés organiques, section on vegetable chemistry. *Jahres-Bericht* **14**, 237.
- BLOMBERG, S., BRACKMANN, C., GUSTAFSON, J., ALD’N, M., LUNDGREN, E. & ZETTERBERG, J. 2015 Real-Time Gas-Phase Imaging over a Pd(110) Catalyst during CO Oxidation by Means of Planar Laser-Induced Fluorescence. *ACS Catalysis* **5** (4), 2028–2034.
- BLOMBERG, S., HEJRAL, U., SHIPILIN, M., ALBERTIN, S., KARLSSON, H., HULTEBERG, C., LÖMKER, P., GOODWIN, C., DEGERMAN, D., GUSTAFSON, J., SCHLUETER, C., NILSSON, A., LUNDGREN, E. & AMANN, P. 2021 Bridging the Pressure Gap in CO Oxidation. *ACS Catalysis* **11** (15), 9128–9135.
- BLOMBERG, S., HOFFMANN, M. J., GUSTAFSON, J., MARTIN, N. M., FERNANDES, V. R., BORG, A., LIU, Z., CHANG, R., MATERA, S., REUTER, K. & LUNDGREN, E. 2013 In Situ X-Ray Photoelectron Spectroscopy of Model Catalysts: At the Edge of the Gap. *Physical Review Letters* **110** (11), 117601.
- BLOMBERG, S., ZETTERBERG, J., GUSTAFSON, J., ZHOU, J., BRACKMANN, C. & LUNDGREN, E. 2016a Comparison of AP-XPS and PLIF Measurements During CO Oxidation Over Pd Single Crystals. *Topics in Catalysis* **59** (5), 478–486.
- BLOMBERG, S., ZHOU, J., GUSTAFSON, J., ZETTERBERG, J. & LUNDGREN, E. 2016b 2D and 3D imaging of the gas phase close to an operating model catalyst by planar laser induced fluorescence. *Journal of Physics: Condensed Matter* **28** (45), 453002.
- BROMBERGER, H., PASSOW, C., PENNICARD, D., BOLL, R., CORREA, J., HE, L., JOHNY, M., PAPADOPOULOU, C. C., TUL-NOOR, A., WIESE, J., TRIPPEL, S., ERK, B. & K’PPER, J. 2022 Shot-by-shot 250 kHz 3D ion and MHz photoelectron imaging using Timepix3. *Journal of Physics B: Atomic, Molecular and Optical Physics* **55** (14), 144001.
- CHAN, W. F., COOPER, G. & BRION, C. E. 1993 The electronic spectrum of carbon

- dioxide. Discrete and continuum photoabsorption oscillator strengths (6–203 eV). *Chemical Physics* **178** (1), 401–413.
- CHANG, S. & THIEL, P. A. 1987 Formation of a metastable ordered surface phase due to competitive diffusion and adsorption kinetics: Oxygen on Pd(100). *Physical Review Letters* **59** (3), 296–299.
- CHANG, S. & THIEL, P. A. 1988a Oxygen on Pd(100): Order, reconstruction, and desorption. *The Journal of Chemical Physics* **88** (3), 2071–2082.
- CHANG, S. & THIEL, P. A. 1988b Summary Abstract: Temperature- and coverage-dependent structures of oxygen on Pd(100). *Journal of Vacuum Science & Technology A* **6** (3), 837–839.
- CHANG, S. L., THIEL, P. A. & EVANS, J. W. 1988 Oxygen-stabilized reconstructions of Pd(100): Phase transitions during oxygen desorption. *Surface Science* **205** (1), 117–142.
- CHEE, S. W., ARCE-RAMOS, J. M., LI, W., GENEST, A. & MIRSAIDOV, U. 2020 Structural changes in noble metal nanoparticles during CO oxidation and their impact on catalyst activity. *Nature Communications* **11** (1), 2133.
- CHIEN, T.-E., HOHMANN, L. & HARDING, D. J. 2022 Near-ambient pressure velocity map imaging. *The Journal of Chemical Physics* **157** (3), 034201.
- CHORKENDORFF, I. & NIEMANTSVERDRIET, J. W. 2017 *Concepts of Modern Catalysis and Kinetics*. John Wiley & Sons.
- EPPINK, A. T. J. B. & PARKER, D. H. 1997 Velocity map imaging of ions and electrons using electrostatic lenses: Application in photoelectron and photofragment ion imaging of molecular oxygen. *Review of Scientific Instruments* **68** (9), 3477–3484.
- ERTL, G. 2001 Heterogeneous catalysis on the atomic scale. *The Chemical Record* **1** (1), 33–45.
- FERNANDES, V. R., GUSTAFSON, J., SVENUM, I. H., FARSTAD, M. H., WALLE, L. E., BLOMBERG, S., LUNDGREN, E. & BORG, A. 2014 Reduction behavior of oxidized Pd(100) and Pd₇₅Ag₂₅(100) surfaces using CO. *Surface Science* **621**, 31–39.
- FRENKEN, J. & GROOT, I., ed. 2017 *Operando Research in Heterogeneous Catalysis, Springer Series in Chemical Physics*, vol. 114. Cham: Springer International Publishing.
- FUKUI, K.-I., MIYAUCHI, H. & IWASAWA, Y. 1996 CO Adsorption and Oxidation on Pd(110)-c(2 × 4)-O by Reflection-Absorption Infrared Spectroscopy. *The Journal of Physical Chemistry* **100** (48), 18795–18801.
- GAO, F., LUNDWALL, M. & GOODMAN, D. W. 2008 Infrared Reflection Absorption Spectroscopy Study of CO Adsorption and Reaction on Oxidized Pd(100). *The Journal of Physical Chemistry C* **112** (15), 6057–6064.
- GAO, F., MCCLURE, S. M., CAI, Y., GATH, K. K., WANG, Y., CHEN, M. S., GUO, Q. L. & GOODMAN, D. W. 2009a CO oxidation trends on Pt-group metals from ultrahigh vacuum to near atmospheric pressures: A combined in situ PM-IRAS and reaction kinetics study. *Surface Science* **603** (1), 65–70.
- GAO, F., WANG, Y., CAI, Y. & GOODMAN, D. W. 2009b CO Oxidation on Pt-Group Metals from Ultrahigh Vacuum to Near Atmospheric Pressures. 2. Palladium and Platinum. *The Journal of Physical Chemistry C* **113** (1), 174–181.
- GAO, F., WANG, Y. & GOODMAN, D. W. 2010 Reply to “Comment on ‘CO Oxidation on Pt-Group Metals from Ultrahigh Vacuum to Near Atmospheric Pressures.

2. Palladium and Platinum⁴⁴. *The Journal of Physical Chemistry C* **114** (14), 6874–6874.
- GOLIBRZUCH, K., SHIRHATTI, P. R., GEWEKE, J., WERDECKER, J., KANDRATSENKA, A., AUERBACH, D. J., WODTKE, A. M. & BARTELS, C. 2015 CO Desorption from a Catalytic Surface: Elucidation of the Role of Steps by Velocity-Selected Residence Time Measurements. *Journal of the American Chemical Society* **137** (4), 1465–1475.
- GOODWIN, C. M., SHIPILIN, M., ALBERTIN, S., HEJRAL, U., LÖMKER, P., WANG, H. Y., BLOMBERG, S., DEGERMAN, D., SCHLUETER, C., NILSSON, A., LUNDGREN, E. & AMANN, P. 2021 The Structure of the Active Pd State During Catalytic Carbon Monoxide Oxidization. *The Journal of Physical Chemistry Letters* **12** (18), 4461–4465.
- GOSCHNICK, J., WOLF, M., GRUNZE, M., UNERTL, W. N., BLOCK, J. H. & LOBODACAKOVIC, J. 1986 Adsorption of O₂ on Pd(110). *Surface Science* **178** (1), 831–841.
- GREENWOOD, T. & KOEHLER, S. P. K. 2021 Nitric Oxide Scattering off Graphene Using Surface-Velocity Map Imaging. *The Journal of Physical Chemistry C* **125** (32), 17853–17860.
- GUSTAFSON, J., BALMES, O., ZHANG, C., SHIPILIN, M., SCHAEFER, A., HAGMAN, B., MERTE, L. R., MARTIN, N. M., CARLSSON, P.-A., JANKOWSKI, M., CRUMLIN, E. J. & LUNDGREN, E. 2018 The Role of Oxides in Catalytic CO Oxidation over Rhodium and Palladium. *ACS Catalysis* **8** (5), 4438–4445.
- HADDEN, D. J., MESSIDER, T. M., LENG, J. G. & GREAVES, S. J. 2016 Note: Velocity map imaging the scattering plane of gas surface collisions. *Review of Scientific Instruments* **87** (10), 106104.
- HANISCO, T. F. & KUMMEL, A. C. 1993 State-resolved photodissociation of nitrous oxide. *The Journal of Physical Chemistry* **97** (28), 7242–7246.
- HARDING, D. J., NEUGEBOHREN, J., HAHN, H., AUERBACH, D. J., KITSOPOULOS, T. N. & WODTKE, A. M. 2017 Ion and velocity map imaging for surface dynamics and kinetics. *The Journal of Chemical Physics* **147** (1), 013939.
- HENDRIKSEN, B. L. M., ACKERMANN, M. D., VAN RIJN, R., STOLTZ, D., POPA, I., BALMES, O., RESTA, A., WERMEILLE, D., FELICI, R., FERRER, S. & FRENKEN, J. W. M. 2010 The role of steps in surface catalysis and reaction oscillations. *Nature Chemistry* **2** (9), 730–734.
- HENDRIKSEN, B. L. M., BOBARU, S. C. & FRENKEN, J. W. M. 2004 Oscillatory CO oxidation on Pd(100) studied with in situ scanning tunneling microscopy. *Surface Science* **552** (1), 229–242.
- HERBSCHLEB, C. T., VAN DER TUIJN, P. C., ROOBOL, S. B., NAVARRO, V., BAKKER, J. W., LIU, Q., STOLTZ, D., CA’AS-VENTURA, M. E., VERDOES, G., VAN SPRONSEN, M. A., BERGMAN, M., CRAMA, L., TAMINIAU, I., OFITSEROV, A., VAN BAARLE, G. J. C. & FRENKEN, J. W. M. 2014 The ReactorSTM: Atomically resolved scanning tunneling microscopy under high-pressure, high-temperature catalytic reaction conditions. *Review of Scientific Instruments* **85** (8), 083703.
- HINES, M. A., MICHELSEN, H. A. & ZARE, R. N. 1990 2+1 resonantly enhanced multiphoton ionization of CO via the E⁺1⁺X⁺1⁺ transition: From measured ion signals to quantitative population distributions. *The Journal of Chemical Physics* **93** (12), 8557–8564.

- HOFFMANN, M. J. & REUTER, K. 2014 CO Oxidation on Pd(100) Versus PdO(101)- $\sqrt{5} \times \sqrt{5}$ R27 $^{\circ}$: First-Principles Kinetic Phase Diagrams and Bistability Conditions. *Topics in Catalysis* **57** (1), 159–170.
- HOFFMANN, M. J., SCHEFFLER, M. & REUTER, K. 2015 Multi-lattice Kinetic Monte Carlo Simulations from First Principles: Reduction of the Pd(100) Surface Oxide by CO. *ACS Catalysis* **5** (2), 1199–1209.
- HUBIN-FRANSKIN, M.-J., DELWICHE, J., LECLERC, B. & ROY, D. 1988 Electronic excitation of carbon dioxide in the 10.5–18 eV range studied by inelastic electron scattering spectroscopy. *Journal of Physics B: Atomic, Molecular and Optical Physics* **21** (19), 3211.
- HURST, J. E., BECKER, C. A., COWIN, J. P., JANDA, K. C., WHARTON, L. & AUERBACH, D. J. 1979 Observation of Direct Inelastic Scattering in the Presence of Trapping-Desorption Scattering: Xe on Pt(111). *Physical Review Letters* **43** (16), 1175–1177.
- INN, E. C. Y., WATANABE, K. & ZELIKOFF, M. 2004 Absorption Coefficients of Gases in the Vacuum Ultraviolet. Part III. CO₂. *The Journal of Chemical Physics* **21** (10), 1648–1650.
- IRIMIA, D., DOBRIKOV, D., KORTEKAAS, R., VOET, H., VAN DEN ENDE, D. A., GROEN, W. A. & JANSSEN, M. H. M. 2009 A short pulse (7 μ s FWHM) and high repetition rate (dc–5kHz) cantilever piezovalve for pulsed atomic and molecular beams. *Review of Scientific Instruments* **80** (11), 113303.
- JANDA, K., HURST, J., BECKER, C., COWIN, J., AUERBACH, D. & WHARTON, L. 1980 Direct measurement of velocity distributions in argon beam-tungsten surface scattering. *Journal of Chemical Physics* **72** (4), 2403–2410.
- JONES, I. Z., BENNETT, R. A. & BOWKER, M. 1999 CO oxidation on Pd(110): a high-resolution XPS and molecular beam study. *Surface Science* **439** (1), 235–248.
- KAWAMATA, H., KOHGUCHI, H., NISHIDE, T. & SUZUKI, T. 2006 Photodissociation of nitrous oxide starting from excited bending levels. *The Journal of Chemical Physics* **125** (13), 133312.
- KIM, M., PAN, L., WEAVER, J. F. & ASTHAGIRI, A. 2018 Initial Reduction of the PdO(101) Surface: Role of Oxygen Vacancy Formation Kinetics. *The Journal of Physical Chemistry C* **122** (45), 26007–26017.
- KNUDSEN, J., GALLO, T., BOIX, V., STRIMSHAM, M. D., D’ACUNTO, G., GOODWIN, C., WALLANDER, H., ZHU, S., SOLDEMO, M., LÖMKER, P., CAVALCA, F., SCARDAMAGLIA, M., DEGERMAN, D., NILSSON, A., AMANN, P., SHAVORSKIY, A. & SCHNADT, J. 2021 Stroboscopic operando spectroscopy of the dynamics in heterogeneous catalysis by event-averaging. *Nature Communications* **12** (1), 6117.
- KONDOH, H., TOYOSHIMA, R., MONYA, Y., YOSHIDA, M., MASE, K., AMEMIYA, K. & MUN, B. S. 2016 In situ analysis of catalytically active Pd surfaces for CO oxidation with near ambient pressure XPS. *Catalysis Today* **260**, 14–20.
- KONG, X., ANDERSSON, P. U., THOMSON, E. S. & PETERSSON, J. B. C. 2012 Ice Formation via Deposition Mode Nucleation on Bare and Alcohol-Covered Graphite Surfaces. *The Journal of Physical Chemistry C* **116** (16), 8964–8974.
- KOSTELNÍK, P., SERIANI, N., KRESSE, G., MIKKELSEN, A., LUNDGREN, E., BLUM, V., IKOLA, T., VARGA, P. & SCHMID, M. 2007 The Pd(100)-(5 \times 5)R27 $^{\circ}$ –O surface oxide: A LEED, DFT and STM study. *Surface Science* **601** (6), 1574–1581.

- LADAS, S., IMBIHL, R. & ERTL, G. 1993 The reactivity of high oxygen coverages on Pd(110) in catalytic CO oxidation. *Surface Science* **280** (1-2), 14–22.
- LONG, J., QIU, Z., WEI, J., LI, D., SONG, X., JIN, B. & ZHANG, B. 2021 Liquid-microjet photoelectron imaging spectrometry for liquid aqueous solutions. *The Review of Scientific Instruments* **92** (6), 065108.
- LUNDGREN, E., GUSTAFSON, J., MIKKELSEN, A., ANDERSEN, J. N., STIERLE, A., DOSCH, H., TODOROVA, M., ROGAL, J., REUTER, K. & SCHEFFLER, M. 2004 Kinetic Hindrance during the Initial Oxidation of Pd(100) at Ambient Pressures. *Physical Review Letters* **92** (4), 046101.
- LYKKE, K. R. & KAY, B. D. 1991 Two“photon spectroscopy of N₂: Multiphoton ionization, laser“induced fluorescence, and direct absorption via the a““1'+g state. *The Journal of Chemical Physics* **95** (4), 2252–2258.
- MARS, P. & VAN KREVELEN, D. W. 1954 Oxidations carried out by means of vanadium oxide catalysts. *Chemical Engineering Science* **3**, 41–59.
- MATERA, S., BLOMBERG, S., HOFFMANN, M. J., ZETTERBERG, J., GUSTAFSON, J., LUNDGREN, E. & REUTER, K. 2015 Evidence for the Active Phase of Heterogeneous Catalysts through In Situ Reaction Product Imaging and Multiscale Modeling. *ACS Catalysis* **5** (8), 4514–4518.
- MCGLYNN, S. P., RABALAIS, J. W., McDONALD, J. R. & SCHERR, V. M. 1971 Electronic spectroscopy of isoelectronic molecules. II. Linear triatomic groupings containing sixteen valence electrons. *Chemical Reviews* **71** (1), 73–108.
- MEHAR, V., EDSTRÖM, H., SHIPILIN, M., HEJRAL, U., WU, C., KADIRI, A., ALBERTIN, S., HAGMAN, B., VON ALLMEN, K., WIEGMANN, T., PFAFF, S., DRNEC, J., ZETTERBERG, J., LUNDGREN, E., MERTE, L. R., GUSTAFSON, J. & WEAVER, J. F. 2023 Formation of Epitaxial PdO(100) During the Oxidation of Pd(100). *The Journal of Physical Chemistry Letters* **14** (38), 8493–8499.
- MEHAR, V., KIM, M., SHIPILIN, M., VAN DEN BOSSCHE, M., GUSTAFSON, J., MERTE, L. R., HEJRAL, U., GRÖNBECK, H., LUNDGREN, E., ASTHAGIRI, A. & WEAVER, J. F. 2018 Understanding the Intrinsic Surface Reactivity of Single-Layer and Multilayer PdO(101) on Pd(100). *ACS Catalysis* **8** (9), 8553–8567.
- MOULA, M. G., WAKO, S., CAO, G., KOBAL, I., OHNO, Y. & MATSUSHIMA, T. 2001 Velocity distribution of desorbing CO₂ in CO oxidation on Pd(110) under steady-state conditions. *Applied Surface Science* **169–170**, 268–272.
- MOULA, M. G., WAKO, S., OHNO, Y., U. KISLYUK, M., KOBAL, I. & MATSUSHIMA, T. 2000 Velocity components in the desorbing product CO₂ in CO oxidation over Pd(100) under steady-state conditions. *Physical Chemistry Chemical Physics* **2** (12), 2773–2778.
- NEYER, D. W., HECK, A. J. R. & CHANDLER, D. W. 1999 Photodissociation of N₂O:“J-dependent anisotropy revealed in N₂ photofragment images. *The Journal of Chemical Physics* **110** (7), 3411–3417.
- NISHIDE, T. & SUZUKI, T. 2004 Photodissociation of Nitrous Oxide Revisited by High-Resolution Photofragment Imaging:“ Energy Partitioning. *The Journal of Physical Chemistry A* **108** (39), 7863–7870.
- NORDEN, B. 2014 *Nobel Lectures In Chemistry (2006-2010)*. World Scientific.
- ORTEGA, A., HUFFMAN, F. M. & BRADSHAW, A. M. 1982 The adsorption of CO on Pd(100) studied by IR reflection absorption spectroscopy. *Surface Science* **119** (1), 79–94.

- OUVRARD, A., WANG, J., GHALGAOUI, A., NAVE, S., CARREZ, S., ZHENG, W., DUBOST, H. & BOURGUIGNON, B. 2014 CO Adsorption on Pd(100) Revisited by Sum Frequency Generation: Evidence for Two Adsorption Sites in the Compression Stage. *The Journal of Physical Chemistry C* **118** (34), 19688–19700.
- OZENSOY, E. & GOODMAN, D. W. 2004 Vibrational spectroscopic studies on CO adsorption, NO adsorption CO + NO reaction on Pd model catalysts. *Physical Chemistry Chemical Physics* **6** (14), 3765–3778.
- RÄMISCH, L., GERICKE, S. M., PFAFF, S., LUNDGREN, E. & ZETTERBERG, J. 2022 Infrared surface spectroscopy and surface optical reflectance for operando catalyst surface characterization. *Applied Surface Science* **578**, 152048.
- RAVAL, R., HAQ, S., HARRISON, M. A., BLYHOLDER, G. & KING, D. A. 1990 Molecular adsorbate-induced surface reconstruction: CO/Pd{110}. *Chemical Physics Letters* **167** (5), 391–398.
- REDHEAD, P. A. 1962 Thermal desorption of gases. *Vacuum* **12** (4), 203–211.
- RETTNER, C. T., AUERBACH, D. J., TULLY, J. C. & KLEYN, A. W. 1996 Chemical Dynamics at the Gas/Surface Interface. *The Journal of Physical Chemistry* **100** (31), 13021–13033.
- VAN RIJN, R., BALMES, O., FELICI, R., GUSTAFSON, J., WERMEILLE, D., WESTERSTRÖM, R., LUNDGREN, E. & FRENKEN, J. W. M. 2010 Comment on “CO Oxidation on Pt-Group Metals from Ultrahigh Vacuum to Near Atmospheric Pressures. 2. Palladium and Platinum“. *The Journal of Physical Chemistry C* **114** (14), 6875–6876.
- RIJN, R. v., BALMES, O., RESTA, A., WERMEILLE, D., WESTERSTRÖM, R., GUSTAFSON, J., FELICI, R., LUNDGREN, E. & FRENKEN, J. W. M. 2011 Surface structure and reactivity of Pd(100) during CO oxidation near ambient pressures. *Physical Chemistry Chemical Physics* **13** (29), 13167–13171.
- RINNEN, K., BUNTINE, M. A., KLINER, D. A. V., ZARE, R. N. & HUO, W. M. 1991 Quantitative determination of H₂, HD, and D₂ internal-state distributions by (2+1) resonance-enhanced multiphoton ionization. *The Journal of Chemical Physics* **95** (1), 214–225.
- ROGAL, J., REUTER, K. & SCHEFFLER, M. 2007a First-Principles Statistical Mechanics Study of the Stability of a Subnanometer Thin Surface Oxide in Reactive Environments: CO Oxidation at Pd(100). *Physical Review Letters* **98** (4), 046101.
- ROGAL, J., REUTER, K. & SCHEFFLER, M. 2007b CO oxidation at $\text{Pd}(100)$: A first-principles constrained thermodynamics study. *Physical Review B* **75** (20), 205433.
- ROGAL, J., REUTER, K. & SCHEFFLER, M. 2008 CO oxidation on Pd(100) at technologically relevant pressure conditions: First-principles kinetic Monte Carlo study. *Physical Review B* **77** (15), 155410.
- SALMERON, M. & SCHLÖGL, R. 2008 Ambient pressure photoelectron spectroscopy: A new tool for surface science and nanotechnology. *Surface Science Reports* **63** (4), 169–199.
- SERIANI, N., HARL, J., MITTENDORFER, F. & KRESSE, G. 2009 A first-principles study of bulk oxide formation on Pd(100). *The Journal of Chemical Physics* **131** (5), 054701.
- SHIPILIN, M., GUSTAFSON, J., ZHANG, C., MERTE, L. R., STIERLE, A., HEJRAL, U., RUETT, U., GUTOWSKI, O., SKOGLUNDH, M., CARLSSON, P.-A. & LUNDGREN,

- E. 2015 Transient Structures of PdO during CO Oxidation over Pd(100). *The Journal of Physical Chemistry C* **119** (27), 15469–15476.
- SHIPILIN, M., HEJRAL, U., LUNDGREN, E., MERTE, L. R., ZHANG, C., STIERLE, A., RUETT, U., GUTOWSKI, O., SKOGLUNDH, M., CARLSSON, P.-A. & GUSTAFSON, J. 2014 Quantitative surface structure determination using in situ high-energy SXRD: Surface oxide formation on Pd(100) during catalytic CO oxidation. *Surface Science* **630**, 229–235.
- SHIPILIN, M., STIERLE, A., MERTE, L. R., GUSTAFSON, J., HEJRAL, U., MARTIN, N. M., ZHANG, C., FRANZ, D., KILIC, V. & LUNDGREN, E. 2017 The influence of incommensurability on the long-range periodicity of the Pd(100)-(5'5)R27'-PdO(101). *Surface Science* **660**, 1–8.
- STARK, G., YOSHINO, K., SMITH, P. L. & ITO, K. 2007 Photoabsorption cross section measurements of CO₂ between 106.1 and 118.7nm at 295 and 195K. *Journal of Quantitative Spectroscopy and Radiative Transfer* **103** (1), 67–73.
- SUZUKI, T., KATAYANAGI, H., MO, Y. & TONOKURA, K. 1996 Evidence for multiple dissociation components and orbital alignment in 205 nm photodissociation of N₂O. *Chemical Physics Letters* **256** (1), 90–95.
- SZANYI, J., KUHN, W. K. & GOODMAN, D. W. 1993 CO adsorption on Pd(111) and Pd(100): Low and high pressure correlations. *Journal of Vacuum Science & Technology A* **11** (4), 1969–1974.
- TAO, F., DAG, S., WANG, L.-W., LIU, Z., BUTCHER, D. R., BLUHM, H., SALMERON, M. & SOMORJAI, G. A. 2010 Break-Up of Stepped Platinum Catalyst Surfaces by High CO Coverage. *Science* **327** (5967), 850–853.
- TAO, F., TANG, D., SALMERON, M. & SOMORJAI, G. A. 2008 A new scanning tunneling microscope reactor used for high-pressure and high-temperature catalysis studies. *Review of Scientific Instruments* **79** (8), 084101.
- TODOROVA, M., LUNDGREN, E., BLUM, V., MIKKELSEN, A., GRAY, S., GUSTAFSON, J., BORG, M., ROGAL, J., REUTER, K., ANDERSEN, J. N. & SCHEFFLER, M. 2003 The Pd(100)“(5'5)R27'-O surface oxide revisited. *Surface Science* **541** (1), 101–112.
- TOYOSHIMA, R., YOSHIDA, M., MONYA, Y., SUZUKI, K., AMEMIYA, K., MASE, K., MUN, B. S. & KONDOH, H. 2013 In Situ Photoemission Observation of Catalytic CO Oxidation Reaction on Pd(110) under Near-Ambient Pressure Conditions: Evidence for the Langmuir–Hinshelwood Mechanism. *The Journal of Physical Chemistry C* **117** (40), 20617–20624.
- TOYOSHIMA, R., YOSHIDA, M., MONYA, Y., SUZUKI, K., MUN, B. S., AMEMIYA, K., MASE, K. & KONDOH, H. 2012 Active Surface Oxygen for Catalytic CO Oxidation on Pd(100) Proceeding under Near Ambient Pressure Conditions. *The Journal of Physical Chemistry Letters* **3** (21), 3182–3187.
- WAKO, S., MOULA, M. G., CAO, G., KIMURA, K., KOBAL, I., OHNO, Y. & MATSUSHIMA, T. 2000 Velocity of Desorbing CO₂ in Steady-State CO Oxidation on Palladium(110):“ Pressure and Temperature Effects. *Langmuir* **16** (6), 2689–2696.
- WEAVER, J. F., CHOI, J., MEHAR, V. & WU, C. 2017 Kinetic Coupling among Metal and Oxide Phases during CO Oxidation on Partially Reduced PdO(101): Influence of Gas-Phase Composition. *ACS Catalysis* **7** (10), 7319–7331.
- WEAVER, J. F., ZHANG, F., PAN, L., LI, T. & ASTHAGIRI, A. 2015 Vacancy-Mediated

- Processes in the Oxidation of CO on PdO(101). *Accounts of Chemical Research* **48** (5), 1515–1523.
- WESTERSTRÖM, R., MESSING, M. E., BLOMBERG, S., HELLMAN, A., GRÖNBECK, H., GUSTAFSON, J., MARTIN, N. M., BALMES, O., VAN RIJN, R., ANDERSEN, J. N., DEPPERT, K., BLUHM, H., LIU, Z., GRASS, M. E., HÄVECKER, M. & LUNDGREN, E. 2011 Oxidation and reduction of Pd(100) and aerosol-deposited Pd nanoparticles. *Physical Review B* **83** (11), 115440.
- WESTERSTRÖM, R., WESTSTRATE, C. J., GUSTAFSON, J., MIKKELSEN, A., SCHNADT, J., ANDERSEN, J. N., LUNDGREN, E., SERIANI, N., MITTENDORFER, F., KRESSE, G. & STIERLE, A. 2009 Lack of surface oxide layers and facile bulk oxide formation on Pd(110). *Physical Review B* **80** (12), 125431.
- WISNIAK, J. 2010 The History of Catalysis. From the Beginning to Nobel Prizes. *Educación Química* **21** (1), 60–69.
- WU, M., TAYLOR, D. P. & JOHNSON, P. M. 1991 Resonance-enhanced multiphoton ionization-photoelectron spectra of CO₂. I. Photoabsorption above the ionization potential. *The Journal of Chemical Physics* **94** (12), 7596–7601.
- YAMANAKA, T. 2008 Angular dependence of rotational and vibrational energies of product CO₂ in CO oxidation on Pd(110). *Physical Chemistry Chemical Physics* **10** (35), 5429–5435.
- YASUI, Y., SAWADA, M., ARUGA, T., TAKAGI, N. & NISHIJIMA, M. 1998 Mechanisms of the CO oxidation on the Pd(110)c(2 × 4)-O surface. *Surface Science* **397** (1), 295–305.
- YU, Y., KIM, D., LIM, H., KIM, G., KOH, Y. E., KIM, D., UEDA, K., HIWASA, S., MASE, K., BOURNEL, F., GALLET, J.-J., ROCHET, F., CRUMLIN, E. J., ROSS, JR., P. N., KONDOH, H., NOH, D. Y. & MUN, B. S. 2019 Operando study of Pd(100) surface during CO oxidation using ambient pressure x-ray photoemission spectroscopy. *AIP Advances* **9** (1), 015314.
- ZETTERBERG, J., BLOMBERG, S., GUSTAFSON, J., SUN, Z. W., LI, Z. S., LUNDGREN, E. & ALDÉN, M. 2012 An in situ set up for the detection of CO₂ from catalytic CO oxidation by using planar laser-induced fluorescence. *Review of Scientific Instruments* **83** (5), 053104.
- ZHANG, J., WANG, Z. & WANG, Z. X. 2011 Adsorption of carbon monoxide on Pd low-index surfaces and (110) reconstructed surface. *Surface and Interface Analysis* **43** (7), 1038–1045.
- ZHENG, G. & ALTMAN, E. 2002a The reactivity of surface oxygen phases on Pd(100) toward reduction by CO. *Journal of Physical Chemistry B* **106** (5), 1048–1057.
- ZHENG, G. & ALTMAN, E. I. 2002b The oxidation mechanism of Pd(100). *Surface Science* **504**, 253–270.
- ZHOU, J., BLOMBERG, S., GUSTAFSON, J., LUNDGREN, E. & ZETTERBERG, J. 2017 Simultaneous Imaging of Gas Phase over and Surface Reflectance of a Pd(100) Single Crystal during CO Oxidation. *The Journal of Physical Chemistry C* **121** (42), 23511–23519.

Part II

Papers

Summary of the papers

Paper 1

Near-ambient pressure velocity map imaging

In this study, we’ve developed an innovative instrument for studying molecular beam surface scattering under near-ambient pressure conditions, bridging the “pressure gap” in catalytic reaction research. Our setup employs velocity-map imaging with electrodes to focus ions and map their velocities at the detector. By placing an aperture between the scattering and detector chambers, we’ve created a differential pumping stage, enabling near-ambient pressure in the scattering chamber without detector damage. Speed resolution is somewhat limited due to electrode compactness but reduces background collisions and retains crucial scattering data. This technique has potential applications in various areas requiring higher pressures, like liquid jets and gas-liquid interfaces.

Paper 2

Time-Resolved Surface Reaction Kinetics in the Pressure Gap

In the present study, we extend the use of our recently developed Near-Ambient Pressure Velocity Map Imaging (NAP-VMI) technique in **Paper 1** to study the kinetics and dynamics of catalytic reactions in the pressure gap. CO scattering and oxidation on the Pd(110) surface with oxygen pressures at the surface up to 1×10^{-5} mbar is investigated, where different metastable surface structures form. We show that NAP-VMI combined with molecular beam and surface scattering techniques allow the direct measurement of time- and velocity-resolved kinetic. The results show that the c(2×4)-O missing row structure formed at low O₂ pressure is highly active for CO oxidation. The CO₂ production is suppressed at higher O₂ pressure due to the number of anti-phase domain boundaries increases, and the missing row sites are filled by O-atoms at O₂ pressures approaching 1×10^{-6} mbar. Filling of these sites by O-atoms reduces the CO surface lifetime, meaning the surface oxide is inactive for CO oxidation. The velocity distribution of the CO₂ products shows the presence of two reaction channels; the time-resolved kinetic measurements show identical reaction time

dependent for the two reaction channels, which we attribute to reactions starting from two distinct but rapidly interconverting CO binding sites.

Paper 3

Bimodel Activity on Heterogeneous Catalysts: CO oxidation on Pd(100)

This work aims to study the CO scattering and oxidation on the Pd(100) surface with NAP-VMI under oxygen pressures at the surface up to 1×10^{-5} mbar, where different metastable surface structures form. Several surfaces (Pd(100) metal phase, PdO(101) single layer, PdO(101) multilayer, and PdO(100) multilayer) are identified during CO oxidation. Among them, the Pd(100) metal phase and the PdO(101) multilayer are active to CO oxidation. Time-resolved kinetic experiments show bimodel activity in surface that have undergone low temperature treatments. To explain this behavior, we have developed two kinetic models to different surface configurations: (1) In the case of the Pd(100) metal phase and the PdO(101) multilayer, these two phases are modeled as distinct active phase for CO adsorption and oxidation. (2) For the Pd(100) metal phase and the PdO(101) single layer, we suggest a adsorption site on the PdO(101) single layer domain boundary for CO oxidation.